Interfacial Dynamics and Applications in Optofluidics

Peng Zhang

Dissertation submitted to the Faculty of the
Virginia Polytechnic Institute and State University
in partial fulfillment of the requirements for the degree of

Doctor of Philosophy
in
Engineering Mechanics

Sunghwan Jung, Chair
Nicole T. Abaid
Raffaella De Vita
Anne E. Staples
Yong Xu

April 14, 2016
Blacksburg, Virginia

Keywords: Optofluidics, Interfacial dynamics, BEM

Interfacial Dynamics and Applications in Optofluidics

Peng Zhang

ABSTRACT

High quality (Q) factor whispering gallery modes (WGMs) can induce nonlinear effects in liquid droplets through mechanisms such as radiation pressure, light scattering, thermocapillarity, Kerr nonlinearity, and thermal effect. However, such nonlinear effects have yet to be thoroughly investigated and compared in the literature. In this study, we first investigate a micron-sized liquid spherical resonator and present an approximated solution for the resonator interface deformation due to the radiation pressure. We then derive an analytical approach that can exactly calculate the droplet deformation induced by the radiation pressure. The accuracy of the analytical solution is confirmed through numerical analyses based on the boundary element method. We show that the nonlinear optofluidic effect induced by the radiation pressure is stronger than the Kerr effect and the thermal effect under a large variety of realistic conditions. Using liquids with ultra-low and experimentally attainable interfacial tension, we further confirm the prediction that it may only take a few photons to produce measurable WGM resonance shift through radiation pressure induced droplet deformation.

Similar to the radiation pressure, the scattering force in the droplet can induce a rotational fluid motion which also leads to the interface deformation. The interface deformation can also be produced by the thermocapillarity as a result of the WGM energy absorption and temperature increase. In this study, we provide a numerical scheme to calculate the fluid motion and quantify the nonlinearity induced by the optical scattering force and thermocapillarity. The magnitude of the optofluidic nonlinearities induced by the radiation pressure, thermocapillary effect, light scattering and Kerr effect are compared. We show that the radiation pressure due to the WGM produces the strongest nonlinear optofluidic effect.

This research received support from the National Science Foundation (CBET 1438112).

Interfacial Dynamics and Applications in Optofluidics

Peng Zhang

GENERAL AUDIENCE ABSTRACT

It has been discovered that light can induce fluid motion. In this dissertation, we focus on a whispering gallery of light wave that travels in a liquid droplet with a radius of around 100 micron. This light wave has the potential of deforming the droplet surface, which in turn changes the property of the light wave. Theoretical and numerical models will be developed in this work to quantitatively predict this change in the light wave property. We will show that this change is much larger than that caused by any other sources. Our findings may have applications in the area of quantum computation and fluid property measurement.

子曰：“岁寒，然后知松柏之后凋也。”

—《论语•子罕》

Dedication

To my family

Acknowledgments

I would like to acknowledge my adviser Dr. Sunghwan Jung who throughout the last three and a half years provided endless guidance and feedback on my work. I wish to express my gratitude to my committee members for all the helpful discussions and meetings in the progress towards my degree. I also appreciate their comments and suggestions for improving this dissertation. Specifically, I want to thank Dr. Yong Xu for providing insights and guidance on my optofluidics research.

I am deeply grateful to Virginia Tech for providing a great academic environment. During the last five years, I was honored to meet many great teachers in different areas. I learned optimal control from Dr. John Burns, abstract algebra from Dr. Mark Shimozono, nonlinear elasticity from Dr. Romesh Batra, and computational fluid dynamics from Dr. Christopher Roy. I wish to thank the Virginia Tech dining services for providing the best campus food in the country. I also thank the Virginia Tech police department for keeping our campus safe.

Throughout my education in the past twenty years, I have been blessed with the continuous support and encouragement from my family and friends. I truly appreciate their patience and understanding.

Finally, I would like to thank the very beautiful and heartwarming Cassandra, who brought so much joy to my life. She is the best cat I can ever ask for.

ATTRIBUTION

Several professors and colleagues aided in the research behind the work presented in this dissertation. A brief description of their contributions is included here.

Calculations and validations related to the electromagnetic field and optical field are attributed to Dr. Yong Xu, who is currently an Associate Professor at the Bradley Department of Electrical and Computer Engineering at Virginia Tech.

Validations of the fluid dynamics results are done by Dr. Sunghwan Jung, who is currently an Associate Professor at the Department of Biomedical Engineering and Mechanics at Virginia Tech.

The parameters and material properties used in the numerical computations are validated by Aram Lee, who is currently a PhD candidate at the Bradley Department of Electrical and Computer Engineering at Virginia Tech.

Contents

List of Figures

List of Tables

Chapter 1

Introduction

1.1 Optofluidics

When light travels through a fluid interface, a net force can be produced on the interface. This phenomenon was predicted and explained by J. Thomson and J. Poynting [1] in the early 1900s. The momentum of a photon depends on the refractive index of the medium it is traveling in. For a photon going across a fluid interface, the change in the momentum results in a net pressure on the interface of the fluid, which can induce fluid motion and interface deformation. Such pressure on the interface is named radiation pressure, which was first observed experimentally by A. Ashkin [2]. A focused laser impulse was projected perpendicular to a flat water surface and micron-sized interface deformation was measured, which was caused by the radiation pressure of light.

The analytic expression of the radiation pressure has since been derived and used in theoretical models [3, 4]. The effects of radiation pressure were also observed in different systems [5]. The fluid interface deformation induced by the radiation pressure was observed by Casner and Delville [6] on a near critical system, whose interfacial tension was 10^6 times smaller than that of a water-air interface. The deformed interface shape was also quantitatively predicted by the force balance, which agreed with the measurement very well. Similar systems had since been used in various experiments. Due to the radiation pressure driven fluid motion, liquid jets can form and serve as waveguides [7]. The radiation pressure was found to have stabilizing effects on the liquid jets: under strong laser beam, the jet was stable; when the laser was switched off, Rayleigh-Plateau instabilities occurred and the jet broke up into droplets.

Theoretical models were also developed to predict the radiation pressure effect on liquid droplets [8, 9, 10, 11]. In a model developed by Lai et al. [8], the droplet interface shape and the radiation pressure were expanded into spherical harmonic series. Each mode in the series was shown to satisfy a second order ordinary differential equation, and the damping

and spring constants depend on the viscosity and surface tension of the droplet. The model worked well to predict the oscillation of the weakly damped droplet under pulsed laser.

In addition to the radiation pressure, light can also induce a force in the bulk of the fluid, which is known as scattering force. The scattering force is induced by refractive index nonhomogeneities resulting from density fluctuations and suspended solid particles. The magnitude of this volume force depends on the light intensity and the density of scatterers. As a result of this bulk effect, fluid circulations on the scale of the fluid container can be observed [12]. The eddies induced by light scattering were predicted numerically and the effect of the liquid layer thickness was also studied [13].

If high-power, focused laser is used in a liquid system, the thermal effect due to light energy absorption is likely to change the dynamics of the system. When the fluid interface is locally heated, a localized thermocapillary force can be produced, known as the Marangoni effect. It was shown by Baroud et al. [14] that with the help of surfactant, a fluid system can have a Marangoni stress that is a few orders of magnitude stronger than the radiation pressure. This Marangoni stress can be used to manipulate the motion of droplets in microfluidic channels, which may find applications in droplet mixing and droplet separation processes. The Marangoni stress can also induce circulating flow on the droplet interface as well as in the volume, which makes microdroplets very effective mixers. In the work by Grigoriev [15], chaotic advections of different invariant surfaces were analyzed and compared, which showed different mixing properties.

1.2 Optical whispering gallery mode

When sound propagates along a concave surface, it is possible that the sound wave may resonate with itself and decay slowly. This type of sound wave, known as the whispering-gallery wave, has been discovered in many structures, including St Paul's Cathedral in London and the Temple of Heaven in Beijing. This phenomenon in St Paul's Cathedral was first explained mathematically by Lord Rayleigh [16, 17] using his own theory of sound [18]. Rayleigh found that the whispering gallery mode (WGM) of the sound waves stayed very close to the concave surface of the dome and had small mode volumes, thus the sound energy was kept within the vicinity of the dome surface. Rayleigh also found that the intensity of the WGM decayed linearly as the inverse of distance. Compared to the sound intensity decay in free space, which is proportional to the inverse of distance squared, the decay of WGM is much slower. This explained why the sound waves in St Paul's Cathedral could travel long distances in the dome.

The whispering gallery mode can also be formed by light waves, which is the focus of this dissertation. To form WGMs, light waves need to propagate in optical resonators with certain geometry and optical properties. The most commonly used resonator is a dielectric sphere whose refractive index is higher than the surrounding material, as shown in Fig. 1.1.

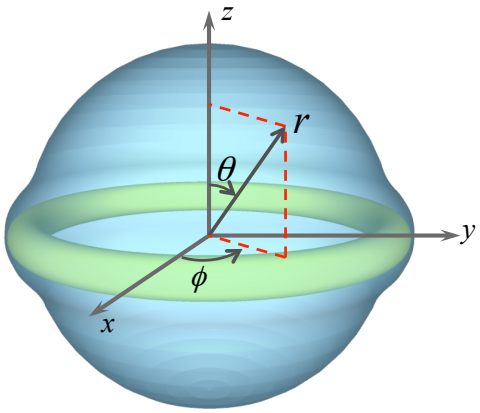

Figure 1.1: A spherical liquid droplet that contains a high-Q WGM circulating along the equator. A Cartesian coordinate (x, y, z) and spherical coordinate (r, θ, ϕ) are defined to assist further analyses.

Light traveling along the equator of the resonator can be confined inside the sphere by the total internal reflection. The analytic expression for the light WGM in spherical resonators can be found in textbooks, e.g. Jackson (1998) [19]. It can be shown that the property of the WGM is determined by three mode numbers, (n, l, m). The number n determines the number of maxima of the electric field intensity along the radial (r-) direction; l determines the maximum number of full wavelengths the light wave can possibly fit along the equator of the sphere; m determines the actual wave number along the equator. Note that the number of maxima of the electric field intensity along the polar (z-) direction equals $(l - m + 1)$. We can show that when $n = 1$, $l \gg 1$ and $m \approx l$, the energy decay out of the sphere is very small and this mode is localized close to the inner boundary of the sphere. Traditionally, modes with mode numbers $n = 1$, $m \approx l \gg 1$ have been defined as WGMs. Unless otherwise specified, we focus our discussions only on WGMs in this dissertation. The electromagnetic field distribution can be explicitly expressed as [19],

$$\begin{aligned} \boldsymbol{E}_{lm} &= g_l(kr)\boldsymbol{X}_{lm}(\theta, \phi), \\ \boldsymbol{H}_{lm} &= -\frac{i}{kZ}\nabla \times [g_l(kr)\boldsymbol{X}_{lm}(\theta, \phi)], \end{aligned} \tag{1.1}$$

where ω and k are the frequency and wave number of the WGM, with $k = k_{co} = \omega_{co}/c$ in the droplet core and $k = k_{cl} = \omega_{cl}/c$ in the cladding region; Z is the impedance of the liquid. $\boldsymbol{X}_{lm}(\theta, \phi)$ is the vector spherical harmonic function,

$$\boldsymbol{X}_{lm}(\theta, \phi) = \frac{1}{\sqrt{l(l+1)}}\boldsymbol{L}Y_{lm}(\theta, \phi), \tag{1.2}$$

where the differential operator $\boldsymbol{L}$ is defined as,

$$\boldsymbol{L} = \frac{1}{i}(\boldsymbol{r} \times \boldsymbol{\nabla}), \tag{1.3}$$

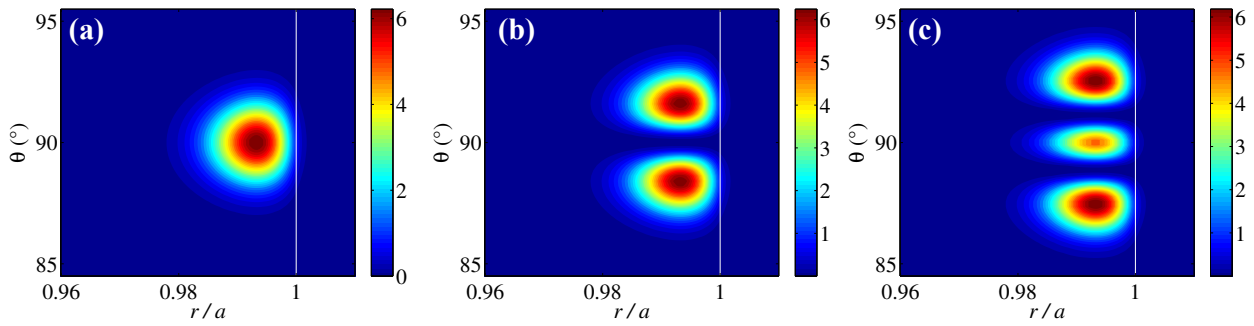

Figure 1.2: Electric field intensity $|\boldsymbol{E}|^2$ distribution on a meridional (ϕ =constant) plane in a spherical resonator with radius $a = 100\,\mu$m. The mode number $l = 1275$ for all cases, while (a) $m = l$, (b) $m = l - 1$, (c) $m = l - 2$. The magnitude of $|\boldsymbol{E}|^2$ is normalized such that the maximum $|\boldsymbol{E}|^2$ on the surface of the sphere (white line) is one.

and the spherical harmonic function is related to the Legendre function (P_l^m) as,

$$Y_{lm}(\theta,\phi) = \sqrt{\frac{2l+1}{4\pi}\frac{(l-m)!}{(l+m)!}} P_l^m(\cos\theta) e^{im\phi}. \tag{1.4}$$

The vector spherical harmonic function defined in Eq. (1.2) satisfies the orthogonality property,

$$\int \boldsymbol{X}^*_{l'm'} \boldsymbol{X}_{lm}\, d\Omega = \delta_{l'l}\delta_{m'm}. \tag{1.5}$$

In Eq. (1.1), $g_l(kr)$ is either the spherical Bessel function (if in the core phase) or the spherical Hankel function (if in the cladding phase),

$$g_l(kr) = \begin{cases} A_{co} j_l(k_{co} r), & r \le a \\ A_{cl} h_l^{(1)}(k_{cl} r), & r > a \end{cases} \tag{1.6}$$

where A_{co} and A_{co} are two constants to be determined by the continuity of the tangential components of $\boldsymbol{E}$ and $\boldsymbol{H}$. Assuming no interfacial current, $\boldsymbol{E}$ and $\boldsymbol{H}$ satisfy,

$$\begin{aligned} \boldsymbol{n} \times (\boldsymbol{E}^{co}_{lm} - \boldsymbol{E}^{cl}_{lm}) &= \boldsymbol{0}, \\ \boldsymbol{n} \times (\boldsymbol{H}^{co}_{lm} - \boldsymbol{H}^{cl}_{lm}) &= \boldsymbol{0}, \end{aligned} \tag{1.7}$$

The interface condition also determines the resonance frequency ω of the WGM, which needs to be solved numerically. We denote the WGM in Eq. (1.1) as $|l, m\rangle$. Once the WGM frequency is known, we can readily determine the field distribution of the WGM using Eq. (1.1). An example of the WGM electric field distribution in a spherical resonator is shown in Fig. 1.2 for different mode numbers. The electric field intensity $|\boldsymbol{E}|^2$ is computed by Eq. (1.1), which exhibits $(l - m + 1)$ maxima along the polar (z-) direction.

The resonance frequency ω of the WGM depends on the frequency of light, the geometry of the resonator as well as the refractive index of the material. The refractive index of the material can be affected by a number of conditions. The temperature of the material can induce a change in refractive index (Δn) as,

$$\Delta n = \frac{dn}{dT}\Delta T, \tag{1.8}$$

where (dn/dT) is the thermal refractive index coefficient [20]. The refractive index is also dependent on the magnitude of the electric field ($\boldsymbol{E}$), which is called the Kerr effect [21],

$$\Delta n = \frac{3\chi^{(3)}}{4}|\boldsymbol{E}|^2, \tag{1.9}$$

where $\chi^{(3)}$ is the third order susceptibility of the material. Note that the temperature change (ΔT) in Eq. (1.8), the Kerr effect in Eq. (1.9) and the magnitude of optofluidic effect in general all depend nonlinearly on the electric field magnitude $|\boldsymbol{E}|$. As will be shown in the following Chapters, all of the aforementioned processes can induce a WGM resonance frequency shift. Therefore, in this dissertation we will refer to the aforementioned effects as "nonlinear effects" or "nonlinearities".

A whispering gallery resonator (WGR) can also have shapes of a cylinder, disk or toroid [22]. These geometries can serve as resonators if the geometry can admit a total internal reflection. However, even on a totally reflected boundary, part of the light energy will be leaked out of the resonator, which causes radiative decay of the WGM energy. In order to quantify the ability of a resonator to store energy, people defined a quality factor, Q, which is a ratio of the stored energy in the resonator to the power loss [19]. High Q-factor means more energy can be stored in the resonator compared to power loss. Other types of energy losses, including intrinsic material absorption, surface absorption, and Rayleigh scattering losses all limit the Q value. The Q-factor also depends on the particular mode of WGM. For a spherical resonator, for example, modes with higher mode numbers possess higher Q-factor.

Whispering gallery resonator can be applied in various systems [23, 24, 25, 26]. Photonics filters have been developed based on optical WGRs. Compared with microwave filters, the advantage of WGM filters is that the WGRs can be designed to be tunable in terms of frequency trimming [27, 28].

As a result of the high Q-factors of WGMs, the WGRs can be used as bio-sensors. The WGM biosensors are highly sensitive, nondestructive and not dependent on the substances. When molecules or cells in the substance approach the WGR, the Q-factor changes due to a change in the photon storage time. This change in Q can be detected if the Q of system is high. WGM sensing systems have since been developed for the detection of particles, DNA and protein, etc [29, 30, 31, 32].

WGRs are also effective optical switches, which makes it possible to carry out quantum computation. It has been shown that all-optical nonlinear switches are feasible with high-

Q resonators[33, 34]. An all-optical 'AND' gate was demonstrated numerically by using a microresonator structure with Kerr nonlinearity [35].

Lower threshold lasers were developed based on WGRs, owing to the high Q-factor of WGMs. A WGM laser based on neodymium-doped silica microspheres with absorbed pump power as low as 20 nW was reported [36].

1.3 Boundary element method

Due to the small scales and slow fluid motion of the optofluidic systems, the Reynolds numbers (Re) of most systems are very low. As an estimate, a typical system has a length scale of $L \leq 10^{-4}$ m, fluid velocity magnitude of $U \leq 10^{-3}$ m/s, viscosity of $\mu \geq 1$ mPa·s, and density of $\rho \sim 1 \times 10^3 \text{kg/m}^3$, the resulting Reynolds number is then $Re = \rho UL/\mu \leq 0.01$. Therefore, the fluid motion of such systems is governed by the linearized Navier-Stokes equation (or Stoke's equations),

$$-\nabla p + \mu \nabla^2 \boldsymbol{u} + \boldsymbol{F} = 0, \nabla \cdot \boldsymbol{u} = 0, \tag{1.10}$$

where p, $\boldsymbol{u}$ and $\boldsymbol{F}$ are the pressure, velocity and body force density field in the fluid. As a result of the linearity of the above equations, efficient numerical algorithms have been developed to simulate viscous flow accurately, such as the finite volume method (FVM), finite element method (FEM) and boundary element method (BEM). Among such algorithms, BEM has been widely employed to address interfacial dynamics problems [37, 38, 39]. For example, an axisymmetric BEM program was used to simulate free rising viscous drop oscillation [40] and drop-drop interaction phenomena [41]. A three-dimensional BEM algorithm that incorporates the elastic behavior of the interface was developed to simulate the dynamic deformation of blood cells in shear flow [42]. Similar algorithms have been applied to explain the swimming and feeding of Paramecia in viscous fluid [43]. Relevant to this dissertation, BEM was adopted to predict the fluid dynamics in optofluidics problems [44, 45, 13]. The effects of radiation pressure [44, 45] and light scattering [13] in a two fluid system with a flat interface were simulated by axisymmetric BEM, which agreed well with the experimental measurements.

The BEM has several advantages compared to volume mesh based methods. For example, discretization is required only on the fluid interface and boundary for BEM based algorithms, rather than in the whole fluid domain. Such a discretization scheme can reduce the dimension of the problem by one, and therefore the resulting linear system has size $O(N^2)$, compared to $O(N^3)$ for FVM and FEM. Another advantage of BEM is that since the elements are distributed directly on the fluid interface, the interface is captured more accurately during dynamic responses compared to FVM, where the interface position is inferred from the fluid volume fraction in the cell. Past research have also shown that FVM cannot preserve the volume of the fluid very well, whereas for BEM the Green's functions satisfy the continuity condition naturally.

There are also noticeable disadvantages of BEM. The linear system matrices generated by BEM are densely populated, which makes it more computationally expensive compared to FVM with the same size. The biggest challenge comes from the singularities of the Green's functions used in BEM. As the Gauss points get closer to a collocation point, the Green's functions may exhibit weak, strong or hyper singularities, depending on the order of derivatives. As a result, the singular integrals must be converted to Cauchy principal value integrals and Hadamard finite part integrals [46], which treat the singularity analytically.

For a two-phase fluid system with a sharp interface in a three-dimensional domain, Eq. (1.10) can be converted to the following boundary integral equation (BIE),

$$u_j(\boldsymbol{x}_0) = b_1 \int_S G_{ji}(\boldsymbol{x}_0, \boldsymbol{x}) f_i(\boldsymbol{x})\, dS(\boldsymbol{x}) + b_2 \int_S u_i(\boldsymbol{x}) K_{ijm}(\boldsymbol{x}_0, \boldsymbol{x}) n_m(\boldsymbol{x})\, dS(\boldsymbol{x}) + b_1 \int_V G_{ji}(\boldsymbol{x}_0, \boldsymbol{x}) F_i(\boldsymbol{x})\, dV(\boldsymbol{x}), \tag{1.11}$$

where $b_1 = -1/(4\pi\mu_1(1+\lambda))$, $b_2 = (1-\lambda)/(4\pi(1+\lambda))$, $\lambda = \mu_2/\mu_1$ is the viscosity ratio of the two phases; $\boldsymbol{f}$ is the total stress on the interface; "S" denotes the interface of the system. The integrals in Eq. (1.11) can be evaluated on each boundary element numerically by the Gauss quadrature. Equation (1.11) can be further simplified before numerical discretization is applied if the problem exhibit some degree of symmetry, e.g., periodic flow and axisymmetric flow. Such simplifications are necessary for a number of reasons. First, the size or dimension of the problem will be reduced. In the case of a periodic flow, the fluid domain in each direction is reduced in size and thus less elements are required to resolve the boundary. For axisymmetric flow, the elements are necessary only on a meridional plane, and thus the dimension is reduced by one. Another advantage with axisymmetric formulation is that by reducing the dimension of the problem, the Green's functions exhibit lower degrees of singularities.

The numerical details of the algorithms including the derivations of the axisymmetric BEM will be explained for specific problems in the following chapters.

1.4 Overview

In this dissertation, we will focus on investigating the optofluidic effects of WGMs in spherical liquid resonators. Since WGMs are essentially electromagnetic waves, the effects of radiation pressure, light scattering and thermocapillarity are expected to exist. Thermal expansion and refractive index change are also expected in the system. This dissertation will be organized as follows.

In Chap. 2, we focus on spherical liquid droplets that support high-Q WGMs. We provide an order of magnitude calculation for the interface deformation induced by the radiation pressure. The distribution of the WGM in the droplet will be computed with appropriate

boundary conditions. The radiation pressure resulting from the WGM is expected to deform the droplet interface. The deformed interface shape will be estimated as an ellipsoid. We will obtain the magnitude of the interface deformation from the force balance on the interface.

In Chap. 3, the exact solution of the system under the radiation pressure will be derived. The exact solutions of the droplet deformation as well as the temperature field distribution will also be provided numerically by BEM. As a result of geometry change, the resonance frequency of the WGM is expected to shift. The nonlinearity induced by the radiation pressure will be compared with the temperature effect and Kerr effect.

In Chap. 4, a new boundary integral equation that incorporates the radiation pressure, scattering force and thermocapillary effect will be derived in an axisymmetric domain. The scattering force induced by the WGM can drive the fluid flow along the equator of the drop. The circulation of the fluid can then lead to droplet interface deformation due to the centrifugal effect. The thermocapillary effect due to laser heating will also be considered in the discussion. Finally, all the optofluidic effects and the Kerr effect will be compared. The optofluidic effect is expected to be stronger in certain systems.

Finally, the results presented in this dissertation will be discussed in Chap. 5. A list of future work will also be suggested.

Chapter 2

Analysis of radiation pressure induced Nonlinear Optofluidics[1]

2.1 Abstract

We analyze a nonlinear optofluidic process where nonlinearity is induced by the interplay between optical field and liquid interface. Specifically, guided optical waves generate radiation pressure on the liquid interface, which can in turn distort the liquid interface and modify the properties of the optical field. We analyze a nonlinear optofluidic process associated with a high quality (Q) factor whispering gallery mode (WGM) in a liquid droplet. Similar to Kerr effects, the WGM can produce a frequency shift proportional to the WGM power. Using liquid properties that are experimentally attainable, we find that it may only take a few photons to generate measurable WGM resonance shift. Such a possibility may eventually lead to nonlinear optics at single photon energy level.

2.2 Introduction

Optofluidics [47, 48, 49, 50, 51, 52] and optomechanics [53, 54, 55] have recently emerged as two important areas of research. Optofluidics aims to synergize microfluidics and optics to achieve novel functionalities including reconfigurable optical systems [47, 48], integrated optics [49, 50], lasers [51], and sensing [52]. Optomechanics, on the other hand, involves the dynamic interplay between optical field and mechanical motion [53, 54, 55]. To date, most

[1]Reprinted with permission from: [Yong Xu, Peng Zhang, Sunghwan Jung, and Aram Lee, Opt. Express 22, 28875 (2014). DOI: 10.1364/OE.22.028875]

optomechanics-related research utilizes solid resonators [56, 57, 58]. Only a limited number of studies investigated the mechanical interaction between optical field and fluids [2, 59, 60, 8, 6, 61]. The earliest example is perhaps the classic work in [2], where the authors used a focused high power laser beam to create a bulge over a flat air-liquid interface. Similarly, in [60, 8], the authors used a high power laser beam focused onto a liquid droplet to distort its interface. More recently, optical radiation pressure was used in [6] to distort a flat liquid interface and form a tunable lens. By using a liquid mixture with extremely small interfacial tension, which can occur near the critical temperature of phase transition, it is possible to significantly reduce the optical power required for large interface distortion [6, 61, 5]. Additionally, stimulated Brillouin scattering in a hollow capillary tube filled with liquid has been reported recently [62]. The existence of high-Q whispering gallery mode (WGM) in an all-liquid droplet has also been experimentally confirmed [63, 64]. The focus of this work, however, is distinct from existing studies. Specifically, our goal is to demonstrate that under appropriate conditions, the dynamic interplay between optical force and liquid interface can lead to processes that are very similar to classical third-order nonlinear processes such as Kerr effects and optical solitons. As will be made clear in this work, a defining feature of these nonlinear optofluidic processes is that the nonlinearity arises from the distortion of liquid interfaced induced by optical radiation pressure.

To analyze nonlinear optofluidic processes, it is necessary to solve the optical equations (e.g., Maxwells equations) and the fluidic equations (e.g., Navier-Stokes equations) in a self-consistent manner, where optical radiation pressure must be balanced by fluidic forces such as surface tension and buoyancy. Consequently, by tuning fluid parameters such as surface tension and density, one should be able to modulate and control the effective strength of optofluidic nonlinearity. This is in sharp contrast with traditional nonlinear optics, where nonlinear susceptibility (e.g., $\chi^{(2)}$ or $\chi^{(3)}$) is an intrinsic material property and cannot be easily tuned. Furthermore, by using liquids with low surface tension, it should be possible to achieve large nonlinearity with low optical power. In fact, in our work, we find that by reducing surface tension to a low but experimentally attainable level, the effective strength of nonlinear optofluidics can be several orders of magnitude stronger than the traditional Kerr effects. To the best of our knowledge, this possibility has never been discussed in existing literature.

A practical example is the system shown in Fig. 2.1, which is based on a liquid droplet that supports high-Q WGMs. In this example, the optical field of the WGM exerts radiation pressure on the droplet surface. Since the direction of radiation pressure always points from the high index core to the low index cladding [8], a bulge should form along the droplet equator. As a result, given sufficiently high optical power, both the effective optical path of the resonator and the corresponding resonance frequency should change. This phenomenon is very similar to the Kerr effect, where high optical power also shifts the effective cavity length by changing the refractive index of the liquid. In this chapter, we derive a closed-form formula that can provide an order of magnitude estimate for this nonlinear optofluidic process. Using common liquid parameters, we find that this nonlinear optofluidic effect can

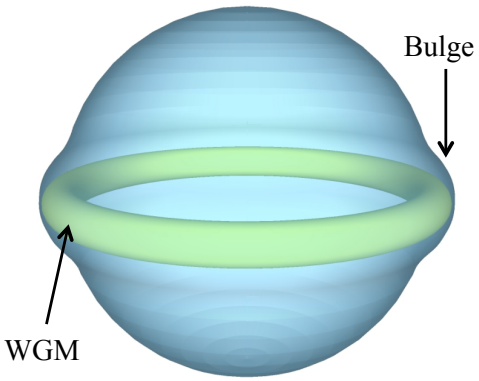

Figure 2.1: A liquid droplet that contains a high-Q WGM circulating along the equator. The radiation pressure of the WGM forms the bulge, which in turn shifts the WGM resonance frequency.

be significantly stronger than the Kerr effect. In fact, for liquids with low but experimentally achievable surface tension, it may even be possible to produce measurable change in WGM resonance frequency at single photon energy level. Such a possibility may ultimately enable us to demonstrate nonlinear interaction between two single photons, which is obviously important for quantum information technology.

2.3 WGM induced droplet deformation

Figure 2.2(a) illustrates the example of radiation pressure induced nonlinear optofluidic processes, where the key element is the high-Q WGM circulating along the equator of a liquid droplet in air. Since the direction of the radiation pressure always points from the high refractive index material to the low index material, the presence of a high-Q WGM would push the spherical droplet surface outwards and consequently enlarge the circumference of the droplets equator. Since radiation pressure is proportional to the optical power carried by the WGM, under the limit of small droplet deformation, we expect that the equator circumference should increase linearly as a function of WGM power and shift the WGM resonance frequency as a direct result. This phenomenon is very similar to the Kerr effect. In the following analysis, we establish an analytical framework and provide an order of magnitude estimate for the frequency shift associated with this nonlinear optofluidic process. Our analysis suggests that the effective strength of the aforementioned nonlinear optofluidic process can be several orders of magnitude larger than the traditional Kerr effect.

The starting point of our analysis is the Young-Laplace equation. We assume a small Bond number, i.e., buoyant force is much smaller than surface-tension force and is ignored. As a result, we find:

$$\Delta p + p_{\text{opt}} = 2\sigma\bar{\kappa}, \tag{2.1}$$

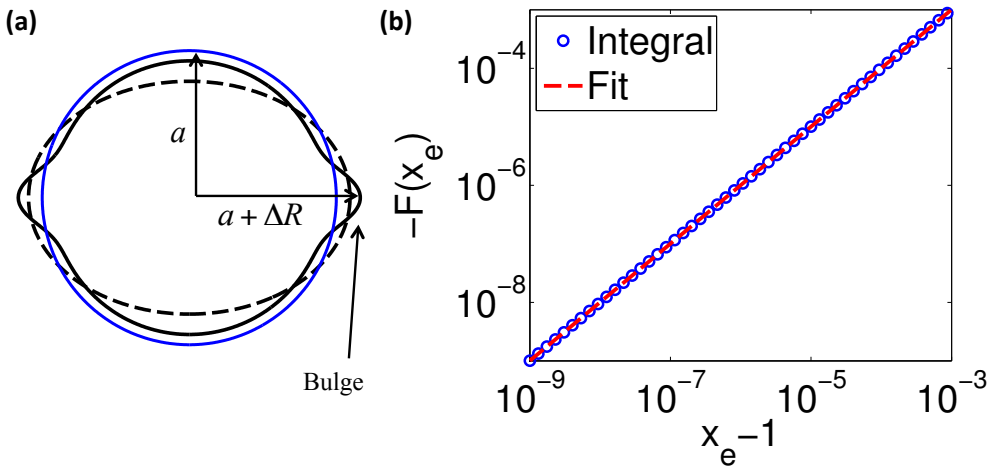

Figure 2.2: (a) A liquid droplet with a high-Q WGM circulating near its equator. The radiation pressure of the WGM deforms the original spherical droplet (the blue circle) and generates the bulge (the solid black line), which is approximated as an oblate spheroid (the dashed black line). The normalized equator radius x_e is defined as the ratio of the spheroid radius at the equator ($a + \Delta R$) and the radius of the original sphere a. (b) The integral $F(x_e) = -\int_0^\pi a\bar{\kappa}\left(x_e, \theta\right) Y_{20}\left(\theta\right) \sin\theta d\theta$ (blue circles) as a function of the normalized equator radius x_e. $\bar{\kappa}\left(x_e, \theta\right)$ is given in Eq. (2.5). The dimensionless constant Γ_σ is extracted using Eq. (2.7) and least square fitting (dashed red line).

where Δp represents the pressure difference inside and outside of the droplet, p_{opt} is the radiation pressure generated by the WGM, σ represents the surface tension of the droplet, and $\bar{\kappa}$ is the mean curvature of the droplet. Note that Δp is constant everywhere on the interface, whereas p_{opt} is a function of θ. Equation (2.1) means that the volume pressure difference (Δp) is balanced by the pressure on the droplet surface (surface tension effect plus the radiation pressure). Since our main purpose is to provide an order of magnitude estimate, we take the following steps to simplify our analysis. First, we restrict our considerations to the fundamental transverse electric (TE) mode. Mathematically, this means that the optical field of the WGM can be written as [19]

$$\vec{E}_{\text{lm}}^{\text{TE}} = g_l\left(k_q r\right) \vec{X}_{lm}\left(\theta, \phi\right) e^{-i\omega t} \tag{2.2a}$$

$$\vec{H}_{lm}^{TE} = -\frac{i}{k_q Z_q} \nabla \times \left[g_l\left(k_q r\right) \vec{X}_{lm}\left(\theta, \phi\right) \right] e^{-i\omega t}, \tag{2.2b}$$

where the angular mode number l and m are integers and satisfy $l > 0$ and $-l \leq m \leq l$, ω is angular frequency. The subscript "q" is either "co" if it represents core parameters of the WGM resonator or "cl" if it denotes cladding parameters. For example, k_{co} refers to the optical wave vector within the droplet, and k_{cl} is the cladding wave vector. Similarly, Z_{co} and Z_{cl} represent the impedance of the droplet core and cladding material, respectively. In Eq.(2.2), $\vec{X}_{lm}$ is the vector spherical harmonic function [19] and represents the angular

variation of the WGM. As to the radial profile of the WGM, the function $g_l(k_q r)$ is either the l-th order spherical Bessel function (for core) or the spherical Hankel function of the first kind (for cladding), i.e.,

$$g_l(kr) = \begin{cases} A_{\text{co}} j_l(k_{\text{co}} r), & r \le a \\ A_{\text{cl}} h_l^{(1)}(k_{\text{cl}} r), & r > a \end{cases} \tag{2.3}$$

where a is the radius of the un-deformed sphere. For the fundamental WGM, the $m = l$ mode and the $m = -l$ mode are identical except for the direction of light circulation. For convenience, we only consider the $m = l$ mode and denote it as $|ll\rangle$. Given Eq. (2.2a), the WGM radiation pressure p_{opt} on the droplet interface is given by [8]

$$p_{\text{opt}} = \frac{1}{2}\varepsilon_0 \left(n_{\text{co}}^2 - n_{\text{cl}}^2\right) \left|\vec{E}_{\text{surf}}\right|^2, \tag{2.4}$$

where ε_0 is free space permittivity, n_{co} and n_{cl} represent core and cladding refractive indices, and $\vec{E}_{\text{surf}}$ is the electric field on the droplet surface. From the expression in Eq. (2.2a), we can verify that $\left|\vec{E}_{\text{surf}}\right|^2$, and therefore p_{opt}, depends on θ but not on ϕ. Additionally, for the $|ll\rangle$ mode, $\left|\vec{E}_{\text{surf}}\right|^2$ is symmetric with respect to the equator plane (i.e., $\theta = \pi/2$).

Numerically solving Eq. (2.2) to (2.4) can give us the form of droplet deformation. However, the mathematical process is complex and can obscure the physics. In this work, we emphasize the physical reality and utilize several assumptions to obtain an intuitive estimate of droplet deformation. First, we assume that the droplet deformation can be approximated by an oblate spheroid, as shown in Fig. 2.2(a). This assumption simplifies our analysis considerably. For example, assuming a spheroid shape, the mean curvature of the droplet interface is simply:

$$\bar{\kappa}(x_e, \theta) = \frac{1}{2a}\frac{x_p}{x_e}\frac{2x_e^2 + \left(x_p^2 - x_e^2\right)\sin^2\theta}{\left[x_e^2 + \left(x_p^2 - x_e^2\right)\sin^2\theta\right]^{3/2}}, \tag{2.5}$$

where x_e and x_p are defined as $R(\theta = \pi/2)/a$ and $R(\theta = 0)/a$, which correspond to the normalized droplet radius at the equator ($\theta = \pi/2$) and at the north pole ($\theta = 0$), respectively. (Volume conservation requires $x_e^2 x_p = 1$.) Furthermore, under the spheroid assumption, the WGM resonance shift can be readily estimated using the perturbation theory in [65].

The next step is to expand both sides of Eq. (2.1) using the spherical harmonic function $Y_{LM}(\theta, \phi)$. From symmetry arguments, we can conclude that most of the spherical harmonic expansion coefficients are zero. First, Δp is constant over the droplet interface, whereas both p_{opt} and $\bar{\kappa}$ are independent of ϕ. Therefore, any $M \neq 0$ term must be zero. Additionally, both p_{opt} and $\bar{\kappa}$ are symmetric with respect to $\theta = \pi/2$. Hence, any term with odd L number must also be zero. The first two non-zero terms of spherical harmonic expansion

involve overlap integrals with Y_{00} and Y_{20}, and are given by:

$$2\Delta p + \int_0^\pi p_{opt}(\theta)\sin\theta d\theta = 2\sigma\int_0^\pi \bar{\kappa}(x_e,\theta)\sin\theta d\theta \tag{2.6a}$$

$$\int_0^\pi p_{opt}(\theta)\,Y_{20}(\theta)\sin\theta d\theta = 2\sigma\int_0^\pi \bar{\kappa}(x_e,\theta)\,Y_{20}(\theta)\sin\theta d\theta, \tag{2.6b}$$

where $Y_{20} = \sqrt{5/16\pi}\,(3\cos^2\theta - 1)$. We can physically interpret Eq. (2.6) as follows. Given the presence of radiation pressure, the difference in fluid pressure Δp should be changed by the amount given in Eq. (2.6a). In other words, the reduction in fluid pressure is a constant term that balances the average magnitude of the radiation force (integrated over the entire droplet surface). After subtracting this constant component (i.e., Δp), it is the θ dependence of the radiation pressure that determines droplet deformation. In applying Eq. (2.6b), we essentially use the first non-zero alternating component to estimate the magnitude of droplet deformation. Obviously, to satisfy Eq. (2.1) exactly, the mean curvature must contain higher "frequency" components. However, using the curvature to calculate droplet shape requires double integration, which can be regarded as a low-pass filter that significantly suppresses these higher frequency components. Therefore, it is reasonable to discard the higher order spherical harmonic terms ($L \geq 4$), and use Eq. (2.6) to estimate the magnitude of droplet deformation.

To further simplify Eq. (2.6b), we note that the right hand side of Eq. (2.6b) is a function of x_e only. Multiplying the integral by droplet radius a, we can define a dimensionless parameter $F(x_e) = -\int_0^\pi a\bar{\kappa}(x_e,\theta)\,Y_{20}(\theta)\sin\theta d\theta$ and numerically evaluate it as a function of x_e. The result, which is shown in Fig. 2.2(b), suggests that this integral is almost a perfect linear function of x_e. Thus we introduce a dimensionless parameter Γ_σ as:

$$F(x_e) = -\int_0^\pi a\bar{\kappa}(x_e,\theta)\,Y_{20}(\theta)\sin\theta\, d\theta \approx \Gamma_\sigma(x_e - 1). \tag{2.7}$$

Through least square fitting, we determine the value of Γ_σ to be 1.01.

To obtain a closed form formula, we express $\left|\vec{E}_{\text{surf}}\right|^2$ in Eq. (2.4) as:

$$\left|\vec{E}_{\text{surf}}\right|^2 = \left|\vec{E}_{\text{surf}}^{\text{peak}}\right|^2 f_{lm}(\theta) \tag{2.8}$$

where $\left|\vec{E}_{\text{surf}}^{\text{peak}}\right|^2$ is the maximum value of $\left|\vec{E}\right|^2$ over the droplet surface. Hence $f_{lm}(\theta)$ represents its angular variation and is normalized to one. Then, the left-hand side of Eq. (2.6b) becomes:

$$\int_0^\pi p_{\text{opt}}(\theta)\,Y_{20}(\theta)\sin\theta\, d\theta = \frac{1}{2}\varepsilon_0\left(n_{\text{co}}^2 - n_{\text{cl}}^2\right)\left|\vec{E}_{\text{surf}}^{\text{peak}}\right|^2\int_0^\pi f_{lm}(\theta)\,Y_{20}(\theta)\sin\theta\, d\theta. \tag{2.9}$$

This leads us to introduce another dimensionless parameter Γ_θ^{lm} as:

$$\Gamma_\theta^{lm} = -\frac{n_{\text{co}}a}{\lambda}\int_0^\pi f_{lm}(\theta)\,Y_{20}(\theta)\sin\theta\, d\theta. \tag{2.10}$$

The coefficient $-n_{\rm co}a/\lambda$ is introduced to ensure that Γ_θ^{lm} is dimensionless and remains reasonably close to one. Combining the results in Eqs. (2.6b), (2.7), (2.9) and (2.10), we find that the normalized droplet deformation $(\Delta R/a)$ near the spheroid equator is given by:

$$\frac{\Delta R}{a} = x_e - 1 = \frac{\Gamma_\theta^{lm}\varepsilon_0\lambda}{4\Gamma_\sigma\sigma n_{\rm co}}\left(n_{\rm co}^2 - n_{\rm cl}^2\right)\left|\vec{E}_{\rm surf}^{\rm peak}\right|^2 \tag{2.11}$$

Equation (2.11) relates droplet deformation to the peak electric field intensity on the droplet interface and is the key result of this chapter. In the next section, we consider several examples of liquid droplets and calculate their deformation as a function of optical power associated with the circulating WGM.

2.4 Estimate of nonlinear optofluidic effects based on high-Q WGMs

Using Eq. (2.11), we can calculate the radiation pressure induced WGM frequency shift and quantitatively compare nonlinear optofluidics with the traditional Kerr effect. We choose the following parameters in our calculations. The core index is $n_{\rm co} = 1.33$, the cladding index is $n_{\rm cl} = 1.0$. The droplet radius varies from $10\mu m$ to $400\mu m$. All WGMs are the fundamental TE mode $|ll\rangle$, and their angular momenta l are chosen to ensure that the WGM wavelengths λ are in the vicinity of . Table 1 lists the l and λ of the TE $|ll\rangle$ mode in such droplets with different radii a. The resonance frequencies are obtained by matching transverse field components across the droplet interface [66], which is assumed to be a perfect sphere.

Table 2.1: Angular Mode Number l and Resonance Wavelength λ of WGMs in Liquid Droplets for $\lambda \approx 1.56\,\mu$m.

$a(\mu$m)	10	12	15	18	21	25	30	35
l	48	58	73	89	104	125	151	177
$\lambda(\mu$m)	1.5524	1.5600	1.5696	1.5605	1.5692	1.5662	1.5670	1.5681
$a(\mu$m)	40	45	50	60	70	80	90	100
l	204	230	257	308	362	415	468	520
λ(nm)	1.5618	1.5638	1.5597	1.5687	1.5628	1.5622	1.5620	1.5649
$a(\mu$m)	120	150	200	250	300	400		
l	625	785	1050	1320	1580	2110		
λ(nm)	1.5670	1.5645	1.5650	1.5598	1.5662	1.5672		

Equation (2.11) links droplet deformation with peak surface field intensity, which is unfortunately not directly measurable. Therefore, we need to further relate the peak field intensity

in Eq. (2.11) with the optical power or energy of the circulating WGM. To accomplish this, we take advantage of the fact that the deformation is linearly proportional to $\left|\vec{E}_{\text{surf}}^{\text{peak}}\right|^2$. Specifically, we choose an electric field amplitude such that $\left|\vec{E}_{\text{surf}}^{\text{peak}}\right| = 1$ and calculate the corresponding field distribution, WGM power flux and total energy. Figure 2.3 shows the field distribution and the ϕ component of the Poynting vector of a WGM ($l = 257$) in a droplet with radius $a = 50\ \mu m$. By integrating the Poynting vector across the $\phi = 0$ plane, we can calculate the total optical power carried by the WGM. Similarly, through volume integration of energy density, we can obtain the total energy stored within the WGM. Then, we multiply the electric field intensity with an appropriate normalization factor such that the total power or the energy of the WGM becomes the desired value. This normalization factor is then used to calculate $\left|\vec{E}_{\text{surf}}^{\text{peak}}\right|^2$ associated with the desired WGM power or energy. Once $\left|\vec{E}_{\text{surf}}^{\text{peak}}\right|^2$ is obtained, the only unknown parameter in Eq. (2.11) is the dimensionless factor Γ_θ^{lm}, which can be obtained through numerical integration of Eq. (2.10) and is shown in Fig. 2.3(d).

Using the procedure described above, we set the power associated with the circulating WGM to be 1 W and use Eq. (2.11) to calculate the radiation induced interface deformation for different droplet radius. The results are shown in Fig. 2.4(a). The red circles give the normalized droplet deformation ($\Delta R/a$) induced by the WGM radiation pressure, where we assume the surface tension is that of water ($\sigma = 72\,\text{mN/m}$). The blue and black diamonds represent the estimated Kerr effect in water (blue) and CS2 (black), produced by the same peak surface field $\left|\vec{E}_{\text{surf}}^{\text{peak}}\right|^2$. These estimates are simply obtained by using $\Delta n \approx \chi^{(3)}\left|\vec{E}_{\text{surf}}^{\text{peak}}\right|^2$, where $\chi^{(3)}$ is the third order nonlinear susceptibility of water ($2.5 \times 10^{-22}\,\text{m}^2/\text{V}^2$) or CS2 ($3.1 \times 10^{-20}\,\text{m}^2/\text{V}^2$). Since both $\Delta R/a$ and Δn represent the same physical effects, i.e., the relative change in the optical path of the high-Q resonator, they can be shown in the same figure for direct comparison. Clearly, the nonlinear optofluidic effect is three to five orders of magnitude stronger than the Kerr effect.

Since the nonlinear optofluidic process can be significantly stronger than the Kerr effect, it is worth asking the question: Is it possible to use only a few photons to generate measurable WGM frequency shift? To answer this question, we first calculate the value of $\left|\vec{E}_{\text{surf}}^{\text{peak}}\right|^2$ such that the total WGM energy equals to single photon energy $\hbar\omega$. Then, we substitute this value into Eq. (2.11) and calculate the normalized radius change $\Delta R/a$ induced by the presence of a single photon. Finally, using the perturbation theory results in [65], the WGM frequency shift associated with the deformed spheroid is:

$$\frac{\Delta\omega}{\omega} = -\frac{2l-1}{2\,(l+1)}\frac{\Delta R}{a} \tag{2.12}$$

Combining Eqs. (2.11) and (2.12), we can now calculate the radiation pressure induced

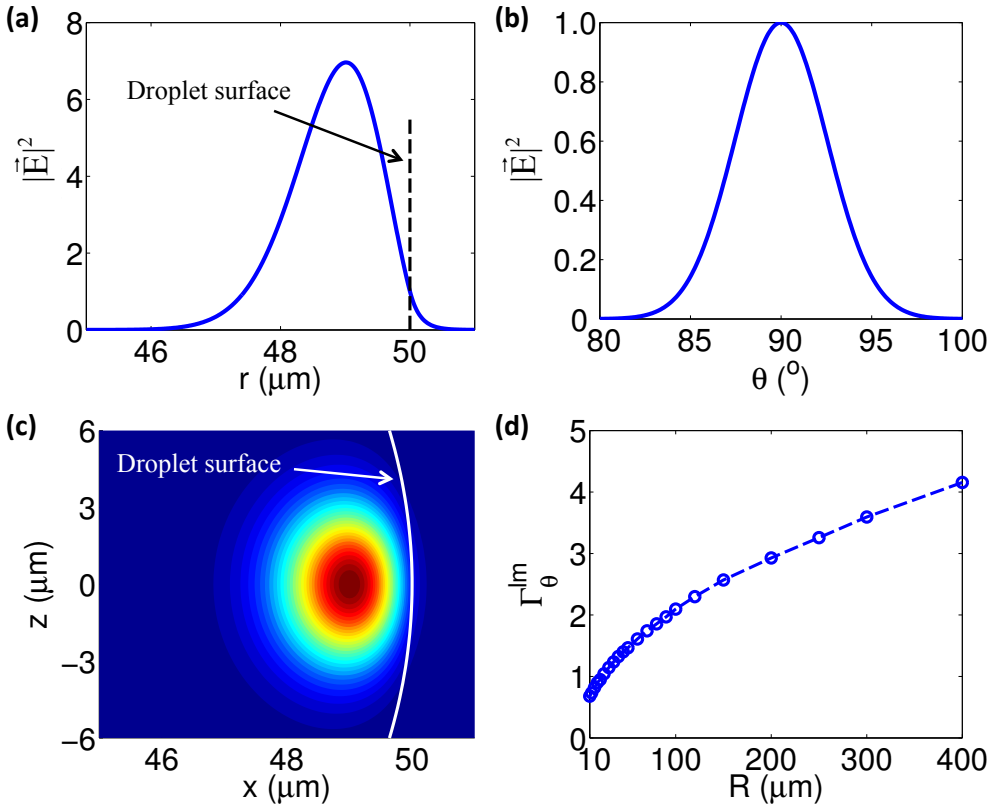

Figure 2.3: (a) The radial dependence of $\left|\vec{E}\right|^2$ of a fundamental TE mode (l =257) in a spherical droplet with radius $a = 50\mu m$. We assume $\left|\vec{E}_{surf}^{peak}\right| = 1$ and take $\theta = \pi/2$ and $\phi = 0$. (b) The angular dependence of $\left|\vec{E}\right|^2$ for the WGM in (a). The value of $\left|\vec{E}\right|^2$ is evaluated over the droplet surface, with $\phi = 0$. Due to our normalization scheme, the curve is also $f_{lm}(\theta)$. (c) The power flux of the WGM in (a) within the $\phi = 0$ plane. Only the $\vec{e}_\phi$ component of the Poynting vector is shown. The white circle represents the droplet surface. (d) The value of Γ_θ^{lm} for the fundamental TE mode $|ll\rangle$ in droplets with different radius. The sphere radii and WGM parameters are listed in Table 1. The Γ_θ^{lm} values (blue circles) are obtained numerically using Eq. (2.10) and simply connected together using the dashed line.

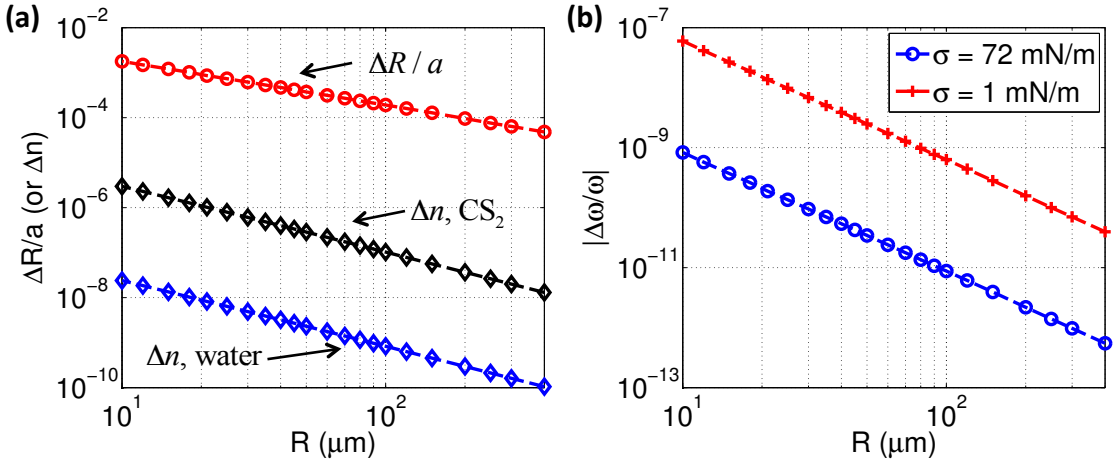

Figure 2.4: (a) Radiation pressure induced droplet deformation ($\Delta R/a$) in droplets with different radii (red circles). The total power of the WGM that circulates along the droplet equator is fixed at 1 W. For comparison, the changes in refractive index (Δn) due to the Kerr effect are shown in the same figure, which are estimated using $\Delta n \approx \chi^{(3)} \left| \vec{E}_{\text{surf}}^{\text{peak}} \right|^2$. The Kerr effects in water and in CS_2 are represented as the blue and black diamonds, respectively. All points are connected by dashed lines. (b) The relative shift in WGM frequency induced by the radiation pressure of a single photon. Two different values are used for surface tension: $\sigma = 72\,\text{mN/m}$ (blue circles), and $\sigma = 1\,\text{mN/m}$ (red crosses). All points are connected by dashed lines.

frequency shift. The results are shown in Fig. 2.4(b). One set of data (blue circles) is obtained using $\sigma = 72\,\mathrm{mN/m}$, which is a typical value for air-liquid interface. The other set of data (red crosses) assumes a low but experimentally achievable surface tension $\sigma = 1\,\mathrm{mN/m}$. Given the fact that WGMs with Q factors as high as 2.3×10^6 have been observed using a liquid resonator [64], Fig. 2.4(b) suggests that one should be able to use only a few photons to produce experimentally observable resonance shift. If one can reduce the surface tension further down to the level of $\sigma = 0.1\,\mathrm{mN/m}$, then the presence of even a single photon can significantly change the characteristics of the liquid droplet resonator.

It is worth remarking that liquid systems with ultralow surface tensions have been experimentally attained using surfactants [67, 68, 45]. For example, by introducing a bimolecular layer of preformed ferric stearate, one can reduce the surface tension of water down to $1\,\mathrm{mN/m}$ [68]. In emulsion or microemulsion systems containing water (a polar fluid) and oil (a nonpolar fluid), surfactants can lower surface tension as small as $1\,\mu\mathrm{N/m}$ at an optimal concentration [67]. Therefore, for these liquid systems with ultralow surface tension, nonlinear optics at single photon energy level should be experimentally feasible.

In our WGM analyses, the effect of gravity is ignored. To justify this choice, we can estimate the Bond number of the liquid droplet. For a sphere with radius a, the gravitational and the surface tension effects can be estimated as $\Delta\rho g \Delta R$ and $\sigma \Delta R/a^2$, respectively. Consequently, the Bond number is simply $B = \Delta\rho g \Delta R/(\sigma \Delta R/a^2)$. For an order of magnitude estimate, we can assume $\Delta\rho \sim 10^3\,\mathrm{kg/m^3}$, $g \sim 10\,\mathrm{m/s^2}$, and $a = 100\,\mu\mathrm{m}$. With these values, even if the surface tension is as low as $\sigma = 1\,\mathrm{mN/m}$, the Bond number remains small ($B \sim 0.1$) and we can safely neglect the gravitational effect in Eq. (2.1).

It is also of interest to briefly consider other types of liquid resonators such as an oil droplet ($n_{co} = 1.45$) immersed in water ($n_{co} = 1.33$). Such a resonator is similar to the one investigated in [63]. As a specific example, we estimate the deformation induced by 1 W WGM power circulating within an oil-in-water droplet with radius $a = 70\,\mu\mathrm{m}$ and interfacial tension $\sigma = 72\,\mathrm{mN/m}$. This resonator supports an TE-polarized WGM with $l = 397$ and resonance wavelength $\lambda = 1.5610\,\mu\mathrm{m}$. Using the procedure described above, we find that 1 W WGM power should induce a relative radius change of $\Delta R/a = 2.94 \times 10^{-4}$. In comparison with the results shown in Fig. 2.4(a), for an water-in-air droplet with identical radius, interfacial tension and WGM power, the deformation is $\Delta R/a = 2.70 \times 10^{-4}$. This result suggests that the conclusions we obtained using water-in-air droplets are broadly applicable to other types of liquid resonators.

Equation (2.11) suggests that the droplet deformation depends on interfacial tension but not on liquid viscosity. This is to be expected, since our discussion is based on static analysis, i.e., the Young-Laplace equation in Eq. (2.1), which does not involve viscosity. We do, however, expect that viscosity should play a role in the dynamics of droplet deformation.

Finally, we point out that the spherical WGM system analyzed here can be connected to liquid-based spheroid resonators. On the one hand, the spherical droplet analyzed in Sect. 2.3 is a special case of the liquid spheroid resonators. On the other hand, a prolate spheroid

resonator with an extremely large major axis can essentially be regarded as an infinitely long dielectric cylinder, which can also support WGM that circulates along the perimeter of the cylinder.

2.5 Conclusion

In this chapter we analyze the possibility of using all liquid systems to achieve nonlinear optical effects with extremely low power threshold. The defining feature of the proposed nonlinear optofluidic processes is the interface deformation due to optical radiation pressure. In particular, we consider a spherical liquid droplet that supports high-Q WGMs. With sufficiently high power, the optical force associated with the circulating WGM could deform the liquid droplet and induce a frequency shift of the WGM resonance. By applying spherical harmonic expansion, we estimate that the radiation pressure induced nonlinearity is several orders of magnitude stronger than the traditional Kerr effect. In fact, we find that by using a liquid system with low but experimentally achievable surface tension, it is possible to produce measurable frequency shift at the energy level of a few photons. Such effect may ultimately lead to nonlinear interactions between two single photons.

Chapter 3

Radiation-pressure-induced nonlinearity in microdroplets[1]

3.1 Abstract

High quality (Q) factor whispering gallery modes (WGMs) can induce nonlinear effects in liquid droplets through mechanisms such as radiation pressure, Kerr nonlinearity, and thermal effects. However, such nonlinear effects, especially those due to radiation pressure, have yet to be thoroughly investigated and compared in the literature. In this study, we present an analytical approach that can exactly calculate the droplet deformation induced by the radiation pressure. The accuracy of the analytical approach is confirmed through numerical analyses based on the boundary element method. We show that the nonlinear optofluidic effect induced by the radiation pressure is stronger than the Kerr effect and the thermal effect under a large variety of realistic conditions. Using liquids with ultralow and experimentally attainable interfacial tension, we further confirm the prediction that it may only take a few photons to produce measurable WGM resonance shift through radiation-pressure-induced droplet deformation.

3.2 Introduction

Optical whispering gallery modes (WGMs) in dielectric microspheres have been extensively investigated for various applications such as quantum electrodynamics [69] and chemical and biological sensing [29, 52]. Due to the high quality factor (Q factor) and small mode volume

[1]Reprinted (abstract/excerpt/figure) with permission from: [Peng Zhang, Sunghwan Jung, Aram Lee, and Yong Xu, Phys. Rev. E 92, 063033 (2015). DOI: http://dx.doi.org/10.1103/PhysRevE.92.063033] Copyright (2015) by the American Physical Society.

of WGMs, many nonlinear optical effects can be significantly enhanced in such resonators [70, 71, 72]. While most existing research used solid structures as WGM resonators, it has been shown that a micro-sized liquid droplet immersed in a fluid with lower index can also serve as a good optical resonator [63, 64].

During the past decade, there has been significant development in the field of optofluidics, where one used fluids to achieve various optical functionalities such as lasing [51], sensing [52], and tunable photonic devices [48]. Optical techniques have also been used in the characterization of liquid properties [73, 74]. The mechanical interplay between optical fields and solid structures has been widely explored in the context of optomechanics [75, 53, 54, 55]. By contrast, the impact of optical force on fluidic systems have only been investigated in a limited number of cases [2, 59, 8, 6, 61, 76, 5]. In general, optical fields can interact with the fluid system through radiation pressure, scattering force or thermal capillary force. Ashkin et al. [2] first demonstrated that a flat liquid surface can be deformed using focused laser pulses. Later experiments on flat and spherical fluid interfaces with different fluid properties confirmed the effect of radiation pressure on fluid interfaces [59, 6, 61, 76, 5]. Brasselet et al. [76], for example, showed that a stable liquid column can be generated and sustained by the radiation pressure on a system with ultralow interfacial tension ($\sim 1.75 \times 10^{-7}\,\mathrm{N/m}$). Theoretical and boundary element models were developed to study fluid motion and interface deformations of a flat fluid interface produced by the radiation pressure [6, 13]. For liquid droplets, analytical theories were also developed to predict the radiation pressure effect [8, 9, 10, 11]. A theoretical description of the droplet shape dynamics was developed in the aforementioned work to quantify the effect of radiation pressure on the drop interface. In a recent work [77], large droplet deformation under optical pressure was also predicted numerically when low interfacial tension was assumed ($\sim 1 \times 10^{-6}\,\mathrm{N/m}$).

Most research to date analyzed the interplay between optical fields and liquids in isolation and did not consider them as a single coupled system. For example, Refs. [8, 9, 6, 10, 11] investigated the deformation of liquid systems due to the radiation pressure of a focused laser beam. The impact of the deformed liquid systems on the optical fields, however, was not considered. In our work in Chap. 2 [78], we first considered optical fields and liquids as a single system coupled together through optical radiation pressure. Under such a framework, we predict many interesting phenomena such as optofluidic solitons and single-photon-level nonlinearity. In particular, we demonstrated that the existence of radiation pressure on micro-sized droplets can lead to a large WGM resonance shift that is analogous to the Kerr effect, which is a classical third-order nonlinear process. However, our previous analysis in Chap. 2 was based on several approximations. The validity of these approximations was not justified through rigorous analyses. Additionally, the exact shape of the deformed droplet was not obtained.

A major objective of this work is to present an analytical framework that can exactly calculate the deformation of the droplets induced by the radiation pressure of the WGMs. The validity of this analytical method shall be confirmed through direct comparison with numerical fluid simulations based on the boundary element method. The results of our ana-

lytical and numerical calculations can also be used to justify the approximation we made in Chap. 2. Additionally, in this study, we quantify the magnitudes of nonlinearities associated with the thermal and Kerr effects, as well as the optofluidic effect induced by the radiation pressure. Specifically, in Sect. 3.3, deformations of the droplet interface are solved analytically by force balance on the interface and numerically by the boundary element method (BEM). Section 3.4 discusses the thermal effects of the WGM on the refractive index and droplet volume using the BEM. Nonlinearities associated with droplet interface deformation and thermal and Kerr effects are compared in Sect. 3.5. Finally, the effect of fluid interface tension and the feasibility of single-photon-level nonlinearities are analyzed in Sect. 3.6.

3.3 Radiation pressure induced droplet deformation

3.3.1 WGM in a droplet

We consider a high-Q WGM circulating along the equator of a high-index liquid droplet (core) immersed in a low-index immiscible fluid (cladding). For a typical drop, its radius a is of the order of $100\,\mu$m, and the density difference $\Delta\rho$ between two fluids is about $200\,\mathrm{kg/m^3}$. Such an optofluidic system possesses a low Bond number ($Bo = \Delta\rho g a^2/\sigma \sim 10^{-3}$, where the surface tension $\sigma \sim 30\,\mathrm{mN/m}$) and a low Reynolds number ($Re = \rho U a/\mu \sim 10^{-2}$, where the characteristic velocity $U = 10^{-3}\,\mathrm{m/s}$ and fluid viscosity $\mu = 13\,\mathrm{mPa\cdot s}$). Given the low Bond and Reynolds numbers, we can safely ignore gravity and inertia effects in our analysis. In this chapter, we denote variables associated with the core phase with subscript "co" and the cladding phase with subscript "cl".

To simplify our analysis, the optical field in the resonator is assumed to be a transverse electric (TE) mode, which can be expressed as [19]

$$\begin{aligned} \vec{E}_{lm} &= g_l(kr)\vec{X}_{lm}(\theta,\phi), \\ \vec{H}_{lm} &= -\frac{i}{kZ}\nabla\times\left[g_l(kr)\vec{X}_{lm}(\theta,\phi)\right], \end{aligned} \tag{3.1}$$

where mode numbers l and m satisfy $l > 0, -l \le m \le l$; ω and k are the frequency and wave number, respectively, of the WGM, where $k = k_{co} = \omega_{co}/c$ in the droplet core and $k = k_{cl} = \omega_{cl}/c$ in the cladding region; Z is the impedance of the liquid; $\vec{X}_{lm}(\theta,\phi)$ is the vector spherical harmonic function; $g_l(kr)$ is either the spherical Bessel function (if in the core phase) or the spherical Hankel function (if in the cladding phase),

$$g_l(kr) = \begin{cases} A_{co} j_l(k_{co} r), & r \le a, \\ A_{cl} h_l^{(1)}(k_{cl} r), & r > a, \end{cases} \tag{3.2}$$

where A_{co} and A_{co} are two constants to be determined by matching the optical field across the drop interface. The field-matching process also gives the frequency ω of the WGM. We

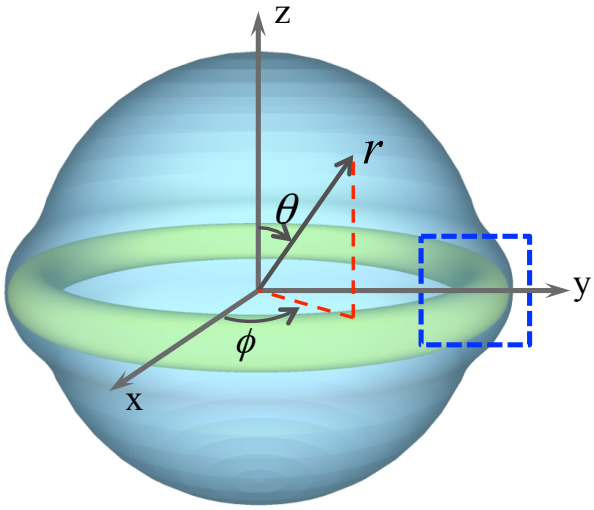

Figure 3.1: Schematic of a droplet containing a high-Q WGM circulating along the equator with a deformed interface. A spherical coordinate system (r, θ, ϕ) is defined to assist further analysis.

denote the WGM in Eq. (3.1) as $|l, m\rangle$. Once the WGM frequency is known, we can readily determine the field distribution of the WGM using Eqs. (1) and (2). For more details, refer to Chap. 2. In this chapter, we are primarily interested in the fundamental WGM with $l = m \gg 1$, which corresponds to a high-Q WGM circulating along the droplet equator, as illustrated in Fig. 3.1.

As demonstrated in Chap. 2 and illustrated in Fig. 3.1, the radiation pressure of the WGM can deform the liquid resonator and produce a large shift in the WGM resonance frequency. The radiation pressure of the WGM can be calculated as (Chap. 2)

$$p_{\text{opt}} = \frac{1}{2}\epsilon_0 \left(n_{co}^2 - n_{cl}^2\right) |\vec{E}_{\text{surf}}|^2, \tag{3.3}$$

where ϵ_0 is the free space permittivity, n_{co} and n_{cl} are refractive indices of the liquid core and cladding, respectively, and $\vec{E}_{\text{surf}}$ is the electric field on the interface. Given the expression in Eq. (3.3), the radiation pressure p_{opt} of the WGM is proportional to the total circulating power (P_{WGM}) associated with the WGM. As in Chap. 2, P_{WGM} can be calculated through a surface integration of the Poynting vector component S_ϕ over a cross section on any $\phi =$ constant plane (as shown by the dashed rectangle in Fig. 3.1),

$$P_{\text{WGM}} = \iint S_\phi dA. \tag{3.4}$$

In Secs. 3.3.2 and 3.3.3, we describe two different approaches that can calculate the interface deformation and fluid motions induced by the radiation pressure on the droplet.

3.3.2 Balanced interface shape

On a stationary fluid interface, the forces on the interface must be balanced by the interfacial tension. When the optical radiation pressure is applied on the interface, the Young-Laplace equation implies

$$\sigma\nabla\cdot\hat{n} = p_{co} - p_{cl} + p_{opt}, \tag{3.5}$$

where σ is the interfacial tension and $\hat{n}$ is the unit normal vector to the surface. Bulk pressures in the core and cladding phases are $p_{co} = p_{co}^0 + \Delta p$ and $p_{cl} = p_{cl}^0$, respectively. Here, p_{co}^0 and p_{cl}^0 are equilibrium pressures in the core and cladding phases before deformation, which satisfy $2\sigma/a = p_{co}^0 - p_{cl}^0$. Δp is the pressure increase inside the droplet caused by the optical pressure, which is determined later. The Young-Laplace equation for a spherical droplet with the radiation pressure becomes

$$\sigma\nabla\cdot\hat{n} = \sigma\frac{2}{a} + \Delta p + p_{opt}\,. \tag{3.6}$$

Assuming axial symmetry and using spherical coordinates, we can describe the interface shape as $r(\theta) = a + \Delta R(\theta)$, where $\Delta R(\theta)$ is the interface deformation. Hence, the interface curvature ($\nabla\cdot\hat{n}$) can be calculated based on the form of $\Delta R(\theta)$. We can further normalize the shape deformation by a as $h(\theta) = \Delta R(\theta)/a$. Under the assumption of small deformation ($h \ll 1$), the Young-Laplace equation (3.6) is linearized as,

$$h''(\theta) + \cot(\theta)h'(\theta) + 2h(\theta) = -\frac{a}{\sigma}(\Delta p + p_{opt}). \tag{3.7}$$

The unknown Δp value in Eq. (3.7) serves as a Lagrange multiplier to ensure the volume conservation of droplet. For a given trial value of Δp, Eq. (3.7) is integrated numerically to produce a solution $h(\theta)$, from which the droplet volume is calculated. Among all the trial values of Δp, the only Δp that satisfies the conservation of the droplet volume is assumed to be the true value.

Due to the linearity of Eq. (3.7), it is clear that $h(\theta)$ is proportional to $1/\sigma$ and the magnitude of p_{opt} ($\propto P_{\mathrm{WGM}}$) (see Appendix A). This relation holds as long as the small deformation assumption is valid.

3.3.3 Boundary Element Method

The motions of the fluid interface and volume are governed by the Navier-Stokes equations. Stokes equations can be applied to this problem as a consequence of the low Reynolds number. Stokes equations and incompressibility condition are written as,

$$-\nabla p + \mu\nabla^2\vec{u} = 0, \nabla\cdot\vec{u} = 0. \tag{3.8}$$

Stokes equations can be solved numerically by the BEM [79]. For a two-phase fluid system with a sharp interface, the interfacial velocity and pressure are related by the following boundary integral equations,

$$\vec{u}(\vec{x}_0) = -\frac{1}{4\pi\mu_{cl}(1+\lambda)}\int_S (\sigma\nabla\cdot\hat{n} - p_{opt})\hat{n}\cdot\boldsymbol{U}(\vec{x}_0,\vec{x}) \times dS(\vec{x}) + \frac{(1-\lambda)}{4\pi(1+\lambda)}\int_S \vec{u}(\vec{x})\cdot\boldsymbol{K}(\vec{x}_0,\vec{x})\cdot\hat{n}(\vec{x})\,dS(\vec{x}), \tag{3.9}$$

where $\lambda = \mu_{co}/\mu_{cl}$ is the viscosity ratio of the core and cladding phases; "S" denotes the interface of the droplet; and position vectors $\vec{x}$ and $\vec{x}_0$ are located on the fluid interface. Also, $\boldsymbol{U}$ and $\boldsymbol{K}$ are Green's functions for Stokes flow in free space,

$$\boldsymbol{U}(\vec{x},\vec{y}) = \frac{1}{d}\boldsymbol{I} + \frac{1}{d^3}\vec{d}\vec{d},\ \boldsymbol{K}(\vec{x},\vec{y}) = -\frac{6}{d^5}\vec{d}\vec{d}\vec{d}, \tag{3.10}$$

with $\vec{d} = \vec{x} - \vec{y}$, $d = |\vec{x} - \vec{y}|$, and $\boldsymbol{I}$ is the identity tensor.

Due to the axisymmetric nature of the geometry and boundary conditions, we can integrate Eq. (3.9) over the ϕ variable analytically to simplify the numerical implementation. The resulting boundary integral equations and Green's functions are well known and available in literature [79, 80].

In our simulations, the fluid interface on the ϕ = constant plane is discretized into N circular arc elements, and $\vec{x}_0$ are located at the center of each element. Assuming constant surface velocity and pressure on each element, Eq. (3.9) can be discretized and written as a linear system relating the unknown interface velocity ($\{v_i\}$) and the known pressure ($\{f_i\} = (\sigma\nabla\cdot\hat{n} - p_{opt})\{\hat{n}_i\}$) vectors,

$$A_{ij}v_j = B_{ij}f_j, \tag{3.11}$$

where $[A_{ij}]$ and $[B_{ij}]$ are $2N \times 2N$ matrices whose entries are integrals of $\boldsymbol{U}$ and $\boldsymbol{K}$ on the interface elements.

The solution to the above linear system gives the velocity at the center of each element on the interface. Velocities at the end points of each element are interpolated by a cubic spline with vanishing derivatives at $\theta = 0, \pi$. The element edges and center displacements are integrated over time by an explicit Euler scheme, i.e., $\Delta\vec{x} = \vec{u}\Delta t$, and a new interface shape is obtained for the following time step. The time step size is chosen by the criteria $\Delta t \le \tau_m = (\mu_{co} + \mu_{cl})l/(2\sigma)$, where l is the element size [39]. This process is iterated until the maximum velocity magnitude $|\vec{u}|$ is sufficiently small.

In our simulations, we find that $N = 128$ elements are sufficient to resolve the interface shape. Each numerical simulation takes about $10 \sim 12$ h of CPU time until a convergent interface shape is obtained.

3.4 Thermal nonlinearity

The optical power (P_{WGM}) carried by the WGM in the resonator can possibly be absorbed by the liquid and converted into thermal energy. Therefore, the droplet temperature may change, which should lead to changes in the optical properties of the droplet as well as the WGM. In this section, we provide an order of magnitude estimate on the thermal effects.

First, we define the steady-state temperature change (T) as the temperature variation induced by the WGM energy. The spatial variation of T in the liquid, which is induced by a heat flux associated with the absorption of the WGM, is governed by the Poisson equation

$$\nabla^2 T(\vec{x}) = g(\vec{x}), \tag{3.12}$$

where $g(\vec{x}) = -\alpha S_\phi/\kappa_{co}$ [44], α is the absorption constant of the droplet core, and κ_{co} is the thermal conductivity of the core liquid. Here we assume that optical absorption occurs predominantly in the droplet core, and all absorbed optical energy is converted to heat.

The solution of temperature field within the droplet core can be easily obtained from the results in [19],

$$\begin{aligned} T(\vec{x}_0) = &-\int_V g(\vec{x}) G(\vec{x},\vec{x}_0) dV(\vec{x}) \\ &-\int_S G(\vec{x},\vec{x}_0)\left[\hat{n}(\vec{x})\cdot\nabla T(\vec{x})\right] dS(\vec{x}) \\ &+\int_S T(\vec{x})\left[\hat{n}(\vec{x})\cdot\nabla G(\vec{x},\vec{x}_0)\right] dS(\vec{x}), \end{aligned} \tag{3.13}$$

where $G = 1/(4\pi|\vec{x}-\vec{x}_0|)$ is the free space Green's function and "V" denotes the core fluid volume. The temperature change in the cladding phase is also governed by Eq. (3.13) with corresponding fluid properties.

In our simulations, we assume the continuity of temperature and heat flux at the droplet interface. We also assume that in the cladding region far away from the droplet, liquid temperature remains unchanged. Similar to the techniques used in Sect. 3.3.3, we also take advantage of the axisymmetry of the problem and introduce a discretization of the boundary on the $\phi =$ constant plane. We can then relate the discretized interface temperature values ($\{T_i\}$) to the known volume integral ($\{I_i^v\}$) at the boundary elements by a linear system similar to Eq. (3.11),

$$H_{ij} T_j = I_i^v, \tag{3.14}$$

where $[H_{ij}]$ is an $N \times N$ matrix whose entries are integrals of the Green's function on the interface elements.

The thermally induced refractive index change (denoted as Δn_T) can be estimated by,

$$\Delta n_T = \frac{dn}{dT} T_{\max}, \tag{3.15}$$

where (dn/dT) is the thermal coefficient of refractive index and $T_{\max}$ is the maximum temperature change in the droplet.

The droplet may also expand in size as its temperature increases. To estimate the effect of thermal expansion, we consider the change in droplet radius near its equator, $\Delta R_T \equiv \Delta R(\theta = \pi/2)/a$. To simplify our analysis, we "overestimate" its magnitude by assuming that the mode volume of the WGM is uniformly heated to the maximum temperature within the droplet ($T_{\max}$). The relative change of radius is then

$$\Delta R_T = \frac{1}{3}\alpha_T T_{\max}, \tag{3.16}$$

where α_T is the thermal expansion coefficient.

3.5 Nonlinear Effects in Liquid Droplets

The properties of the WGMs depend on the liquid refractive indices as well as the size and shape of the resonator. In our studies of nonlinear effects, we choose a liquid system based on an oil droplet immersed in water. The fluid we used for the droplet core is an index-matching fluid (Series AA14500, Cargille Laboratories). Fluid viscosities of the core and cladding media are $\mu_{co} = 13\,\mathrm{mPa}\cdot\mathrm{s}$ and $\mu_{cl} = 1\,\mathrm{mPa}\cdot\mathrm{s}$, and the heat conductivities are $\kappa_{co} = 0.126\,\mathrm{W/m{\cdot}K}$ and $\kappa_{cl} = 0.60\,\mathrm{W/m{\cdot}K}$, respectively. The oil-water interfacial tension is measured by a goniometer (Model 590, ramé-hart instrument co.) to be around $\sigma = 30\,\mathrm{mPa{\cdot}s}$. While this dissertation focuses on analytical and numerical aspects of the system, the material specified here will be used in our future experimental work.

This system has the highest Q factor at the wavelength of $\lambda \approx 700\,\mathrm{nm}$, since optical absorption is lowest at this wavelength. At $\lambda \approx 700\,\mathrm{nm}$, the effective refractive indices of the core and cladding phases are $n_{co} = 1.44$ and $n_{cl} = 1.33$, respectively. We apply the procedure in Chap. 2 to determine the resonance frequency of the WGMs resonator. We first consider the fundamental mode $|l, l\rangle$, which corresponds to an optical field with a single maximum along the polar direction. The angular mode number l's of the WGMs are chosen so that λ's are close to 700 nm. Table 3.1 gives the angular mode number l and the resonance wavelength λ of the WGMs in droplets with different radii a.

Assuming that absorption in the droplet core is the only source of the energy loss, we can estimate the WGM Q-factors of the above resonators to be $Q = 2\pi n_{co}/(\alpha\lambda) \approx 10^8$ with absorption constant $\alpha = 0.125\,\mathrm{m}^{-1}$ (according to the specification of the index matching fluid). The interface deformations of the above resonators are computed using both the analytical method in Sect. 3.3.2 and the numerical method in Sect. 3.3.3. Nonlinearities due to interface deformation, temperature change, and Kerr effect are estimated separately.

Table 3.1: Angular Mode Number l and Resonance Wavelength λ of WGMs in Liquid Droplets.

$a(\mu\text{m})$	400	300	250	200	150	120
l	5145	3847	3204	2569	1918	1529
λ(nm)	699.35	700.66	700.45	698.05	699.95	701.26
$a(\mu\text{m})$	100	80	70	60	50	40
l	1275	1018	889	761	632	504
λ(nm)	699.75	699.65	700.05	699.75	700.55	700.59

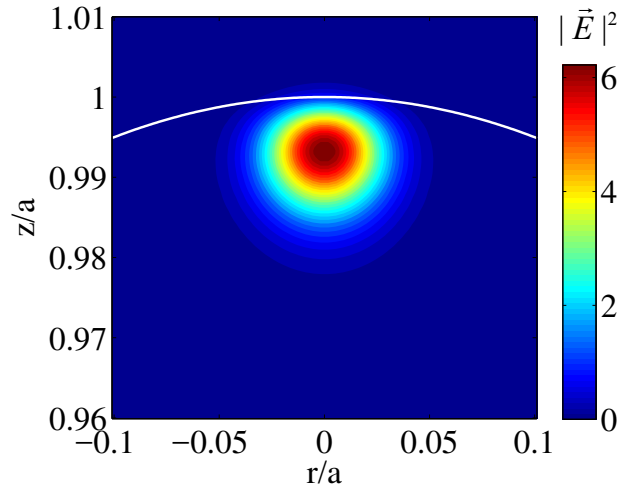

Figure 3.2: $|\vec{E}|^2$ distribution in the droplet on a $\phi =$ constant plane. The electric field has been normalized so that on the interface the maximum intensity $|\vec{E}|^2_{\text{max}} = 1$. The white curve represents the droplet interface.

3.5.1 Nonlinear effects

In this section, we consider nonlinearities associated with the fundamental WGM $|l, l\rangle$, with the mode number l given by Table 3.1. The electric field across the droplet interface is calculated by Eq. (3.1). As an example, the electric field intensity in a droplet with $a = 100\,\mu$m is shown in Fig. 3.2. The total WGM power of the electric field is then given by Eq. (3.4). Since nonlinear effects induced by the radiation pressure are proportional to P_{WGM}, we only need to analyze droplet deformation at a specific WGM power level. In this chapter, the electric field is normalized such that the total WGM power is $P_{\text{WGM}} = 1\,\text{W}$. With known electric field intensity on the interface, droplet interface deformations induced by the radiation pressure are computed by the force balance Eq. (3.7) and BEM Eq. (3.9).

In Fig. 3.3, we compare the interface deformation obtained using the analytical method in

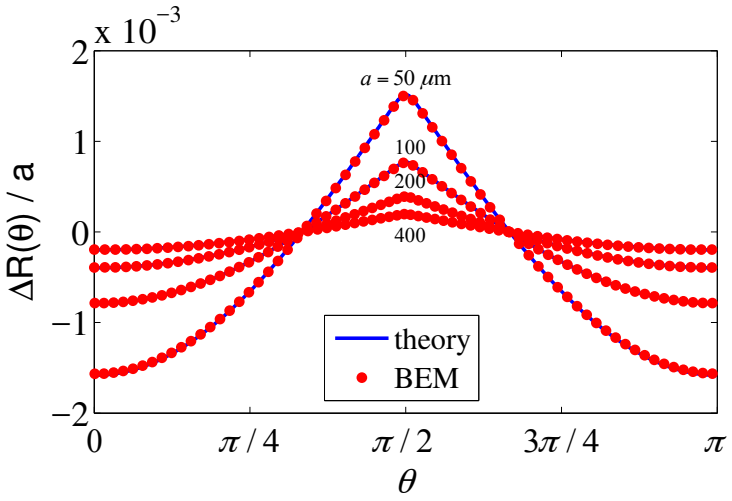

Figure 3.3: Solutions of the balanced interface deformation by the Young-Laplace equation and the BEM simulations for radii $a = 50, 100, 200$, and $400\,\mu$m.

Sect. 3.3.2 and the numerical BEM simulations described in Sect. 3.3.3. The equilibrium interface shapes obtained by the BEM are in excellent agreement with the force balance predictions given by Eq. (3.7). The BEM solutions also produce a velocity distribution in the droplet, as shown in Fig. 3.4.

As discussed in Sect. 3.3.2, the maximum droplet interface deformation $\Delta R/a$ is linearly dependent on the values of $1/\sigma$ and P_{WGM}, which is also implied by the approximated solution in Chap. 2 (Sect. 3.5.2, Eq. (3.17)). Therefore, the interface shapes under arbitrary WGM powers and interfacial tension values can be linearly extrapolated from the solutions in Fig. 3.3.

The temperature change due to the optical absorption of the WGM can be computed numerically as described in Sect. 3.4. Again, we assume that the circulating WGM power is 1 W, and that all optical energy absorbed by the core liquid ($\alpha = 0.125$) is converted to heat. Based on Eqs. (12) to (14), we can calculate temperature distribution within the droplet. The results are shown in Fig. 3.5. Figure 3.6 gives the changes in refractive index and the size of the liquid core as estimated by Eqs. (3.15) and (3.16), where we assume the core liquid possesses a thermal coefficient of $(dn/dT) = -3.9 \times 10^{-4}\,\mathrm{K}^{-1}$, and a thermal expansion coefficient of $\alpha_T = 8 \times 10^{-4}\,\mathrm{K}^{-1}$. In terms of their impact on the WGMs, these two thermal processes are nearly the same, as can be seen from Fig. 3.6.

Kerr effect is a classical third-order nonlinear process, where the material refractive index depends linearly on optical field intensity [81]. For the liquid resonator, the refractive index change as a result of the Kerr effect can be estimated as $\Delta n \approx \chi^{(3)}|\vec{E}|^2_{\mathrm{max}}$, where $\chi^{(3)}$ is the third order nonlinear optical susceptibility, and $|\vec{E}|_{\mathrm{max}}$ is the maximum electric field intensity in the droplet. To provide an order of magnitude estimate of the Kerr effect, we use water

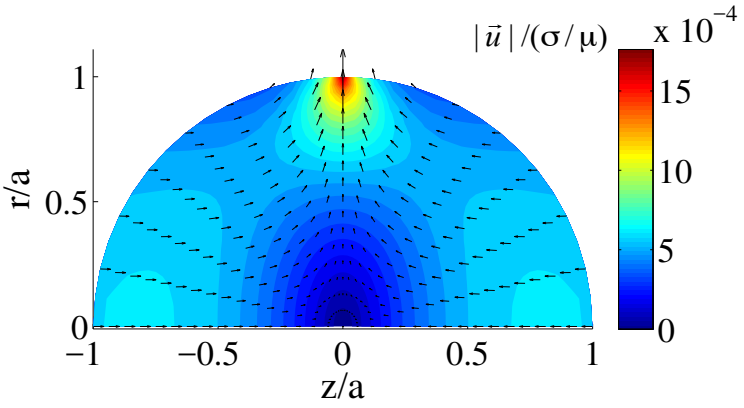

Figure 3.4: Fluid velocity direction (arrows) and magnitude (color) distribution on the $x = 0$ plane at time $t = 0$. Velocity values are normalized by σ/μ.

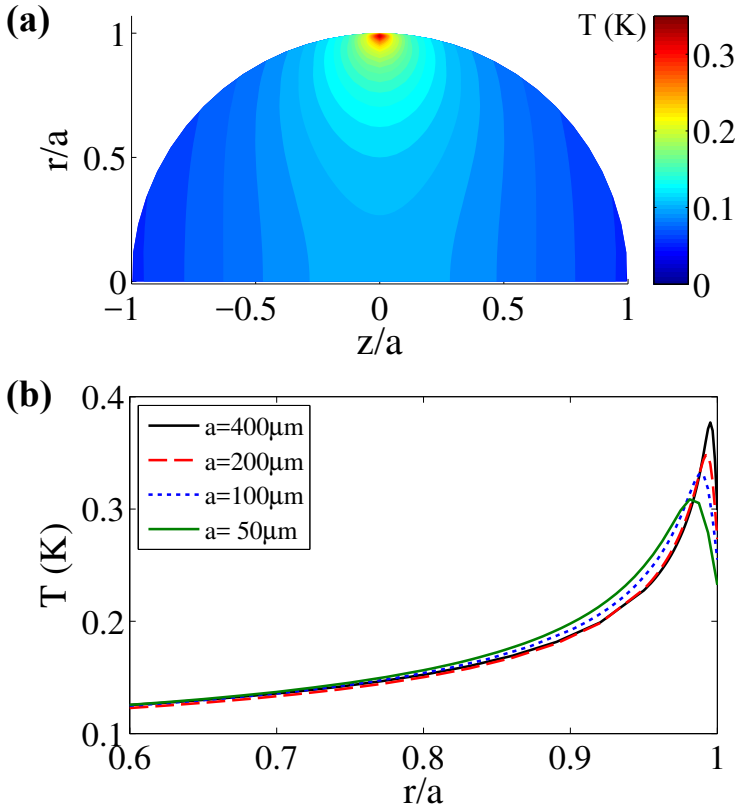

Figure 3.5: Changes in fluid temperature in the liquid core due to optical absorption. (a) Temperature distribution in the $x = 0$ plane for a droplet with radius $a = 100\,\mu$m. (b) Radial temperature distribution at $\theta = \pi/2$ for droplets with radii $a = 50, 100, 200$ and $400\,\mu$m.

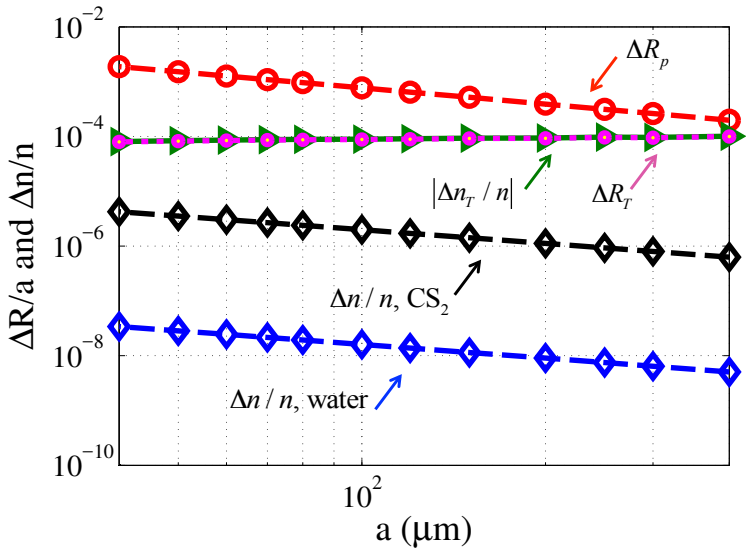

Figure 3.6: Comparison of the strength of nonlinearity due to radiation pressure, thermal effects, and Kerr effect. The vertical axis is either relative deformation at the droplet equator ($\Delta R(\theta = \pi/2)/a$, caused by radiation pressure and thermal expansion), or refractive index changes ($\Delta n/n$, caused by thermo-optic effect and Kerr nonlinearity). Droplet radius changes ΔR_T associated with thermal expansion overlap with the refractive index changes $\Delta n_T/n$ induced by temperature changes.

and carbon disulfide (CS_2) ($\chi^{(3)}_{\text{water}} = 2.5 \times 10^{-22}\,\text{m}^2/\text{V}^2$ and $\chi^{(3)}_{\text{CS}_2} = 3.1 \times 10^{-20}\,\text{m}^2/\text{V}^2$) to calculate the refractive index change due to the Kerr effect.

We now compare the impact of the three nonlinear processes — radiation pressure effect, thermal effects, and Kerr effect — on liquid droplets. Let us define the interface deformation at the equator as $\Delta R(\theta = \pi/2)/a \equiv \Delta R_p$. As shown in Fig. 3.6, interface deformation induced by the radiation-pressure (ΔR_p) is a few orders of magnitude higher than the Kerr effect ($\Delta n/n$). Additionally, for smaller liquid droplets, nonlinearity caused by the radiation pressure is also significantly higher than the thermal nonlinearity. However, for millimeter-sized droplets, the radiation pressure effect and the thermal effects can be comparable in magnitude. However, even for cases where thermal effects are significant, it might be possible to distinguish radiation-pressure effect and thermal effects through direct measurements of the interface deformation. According to Fig. 3.6, for a droplet with 100 μm radius and typical interfacial tension ($\sigma = 30\,\text{mN/m}$), a WGM with 1 W power can deform the droplet radius by approximately 100 nm. Many optical interferometry techniques are capable of measuring this estimated interfacial deformation. For example, the methods reported in Refs. [82, 83, 84] can all measure surface deformation with nanometer or subnanometer spatial resolutions.

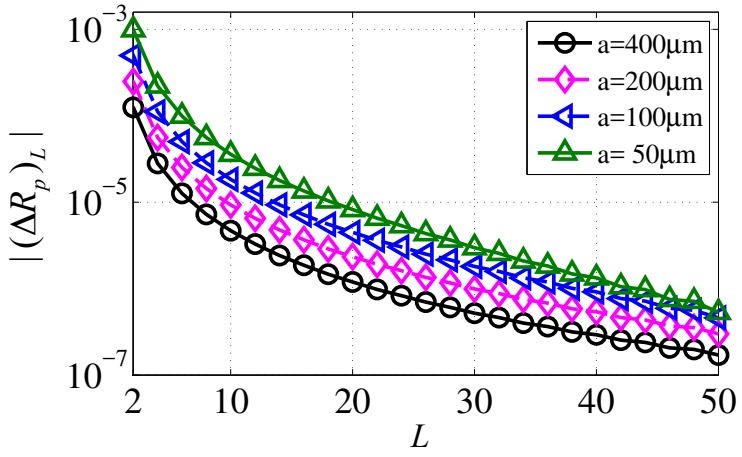

Figure 3.7: Spherical harmonics expanded terms ($|(\Delta R_p)_L|$) in Eq. (3.20b) for four cases shown in Table 3.1. Coefficients with odd indices are zero and are not shown here.

3.5.2 Comparison of the exact solution and the approximate solution

In Chap. 2, we gave an analytical formula that can estimate the magnitude of the nonlinearity induced by the radiation pressure. In that approach, the droplet deformation was approximated by an ellipsoid and the radius change at the equator ($\Delta R(\theta = \pi/2)/a$) was given by

$$\Delta R_p = \frac{\Gamma_\theta^{lm} \epsilon_0 \lambda}{4\Gamma_\sigma \sigma n_{co}} \left(n_{co}^2 - n_{cl}^2\right) |\vec{E}_{\text{surf}}^{\text{peak}}|^2, \tag{3.17}$$

where $\Gamma_\sigma \approx 1.01$ is given by the ellipsoid assumption and Γ_θ^{lm} is associated with the angular dependence of the radiation pressure,

$$\Gamma_\theta^{lm} = -\frac{n_{co} a}{\lambda} \int_0^\pi f_{lm} Y_{20}(\theta) \sin(\theta)\, d\theta, \tag{3.18}$$

where f_{lm} is the normalized radiation pressure whose maximum value on the interface is one. With the help of Clebsch-Gordan coefficients, Eq. (3.18) can be simplified as (Appendix B)

$$\begin{aligned} \Gamma_\theta^{lm} = &-\frac{n_{co} a}{\lambda} \frac{1}{2\pi |\vec{X}_{lm}|_{\max}^2} \left[1 - \frac{3}{l(l+1)}\right] \sqrt{\frac{5}{4\pi}} \\ &\times \langle 2, l; 0, m | l, m \rangle \langle 2, l; 0, 0 | l, 0 \rangle . \end{aligned} \tag{3.19}$$

Note that, taken together, Eqs. (3.17) and (3.19) give an analytical estimate for the droplet deformation induced by the radiation pressure. The accuracy of this analytical approximation is investigated here.

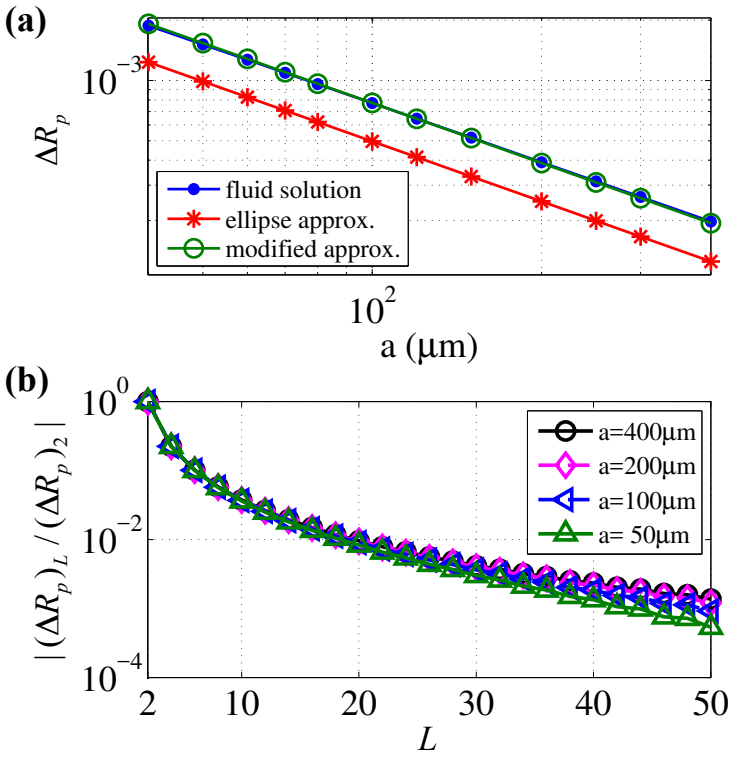

Figure 3.8: (a) Comparison of the maximum interface deformation between exact solutions given by the current work with approximated solutions in Chap. 2. (b) Spherical harmonics expanded terms ($|(\Delta R_p)_L|$) normalized by the first nonzero term $|(\Delta R_p)_2|$.

Table 3.2: The approximate analytic solutions of droplet deformation (ΔR_p according to Eq. (3.17)), and the leading spherical harmonic expansion term ($(\Delta R_p)_2$, due to Y_{20} only) of the exact interface deformation solution.

$a(\mu\text{m})$	ΔR_p	$(\Delta R_p)_2$
400	1.247×10^{-4}	1.246×10^{-4}
200	2.490×10^{-4}	2.488×10^{-4}
100	4.967×10^{-4}	4.962×10^{-4}
50	9.891×10^{-4}	9.882×10^{-4}

The exact interface deformation can be expressed in terms of the spherical harmonics Y_{LM} as,

$$\frac{\Delta R(\theta)}{a} = \sum_{L=2}^{N} \sqrt{4\pi}\Delta_L Y_{L0}(\theta), \tag{3.20a}$$

$$\frac{\Delta R(\pi/2)}{a} = \sum_{L=2}^{N} (\Delta R_p)_L, \tag{3.20b}$$

where $Y_{L0}(\theta)$ is the spherical harmonic function $Y_{L0}(\theta, \phi)$ with $\phi = 0$, Δ_L is the expansion coefficient, and $(\Delta R_p)_L = \sqrt{4\pi}\Delta_L Y_{L0}(\pi/2)$ denotes droplet deformation at the equator due to the Y_{L0} term. Due to the rotational symmetry (with respect to the z axis) and the mirror reflection symmetry (with respect to the $z = 0$ plane), the droplet deformation does not contain any Y_{LM} term with odd L number or with $M \neq 0$. The values of $(\Delta R_p)_L$ up to $L = 50$ are shown in Fig. 3.7 for interface deformations of droplets with four different radii. Note that we must have $(\Delta R_p)_0 = 0$ to satisfy the volume conservation. Figure 3.7 shows that the value of $|(\Delta R_p)_L|$ decreases rapidly as L increases, with $(\Delta R_p)_2$ being the dominant term. A comparison of the $L = 2$ term in Fig. 3.7 with the solution in Eq. (3.17) is shown in Table 3.2. In Fig. 3.8(a), we also compare the exact droplet deformation given by the current work with the approximate solution in Eq. (3.17). The results show that the first-order approximation in Eq. (3.17) can provide a reasonably accurate prediction of the interface deformation caused by the radiation pressure. In fact, if we change the constant Γ_σ in Eq. (3.17) from $\Gamma_\sigma = 1.01$ to $\Gamma_\sigma = 0.643$, the slightly modified analytical formula ("modified approx." in Fig. 3.8(a)) agrees very well with the equator deformation ΔR_p as given by the exact solutions. This excellent agreement can be explained by the observation that for the simulation parameters considered in this work, the interfacial deformation $\Delta R(\theta)/a$ can be factored into a product of the equator deformation ΔR_p and an angular shape function $f(\theta)$, with $f(\theta)$ being mostly independent of parameters such as droplet radius, interfacial tension, and optical power. This observation can be easily confirmed by normalizing various orders of $(\Delta R_p)_L$ with the leading term $(\Delta R_p)_2$, as shown in Fig. 3.8(b). Regardless of droplet radius, the normalized deformation factors, $(\Delta R_p)_L/(\Delta R_p)_2$, are almost identical, which indirectly

confirms the shape independence of the radiation-pressure-induced deformation.

3.6 Single-photon-level nonlinearity

In this section, we discuss perhaps the most important prediction of our theoretical analysis, namely the feasibility of single-photon-level nonlinearity.

As proposed in Chap. 2, for the ultralow interfacial tension fluid systems that have been demonstrated in the past experiments, the radiation pressure induced droplet deformation may lead to a measurable WGM shift at the single-photon energy level. In contrast with our earlier work Chap. 2 based on the approximate solution, here we estimate the magnitude of the WGM resonance shift induced by the radiation pressure using the exact solution presented in Sect. 3.5.

The general framework of our analysis is as follows. First, we expand the exact solution of the deformed droplet using spherical harmonic functions. Then, based on the perturbation theory in [65], we can sum over the frequency shift due to each spherical harmonic term and obtain the total resonance shift for a specific WGM mode $|l, m\rangle$. Mathematically, this means

$$\frac{\Delta\omega}{\omega} = \sum_{L=2,4,6,\ldots}^{\infty} \frac{\Delta\omega_L}{\omega} = -\sum_{L=2,4,6,\ldots}^{\infty} \Delta_L F(L, l, m), \tag{3.21}$$

where the expansion coefficients Δ_L are given in Eq. (3.20a), and $F(L, l, m)$ can be derived as

$$\begin{aligned} F(L, l, m) &= \sqrt{4\pi} \iint |\vec{X}_{lm}|^2 Y_{LM}\, d\Omega \\ &= \left[1 - \frac{L(L+1)}{2l(l+1)}\right] \sqrt{2L+1} \\ &\quad \times \langle L, l; M, m | l, m\rangle \langle L, l; 0, 0 | l, 0\rangle . \end{aligned} \tag{3.22}$$

The expression in Eq. (3.22) is derived in Appendix B. Values of $|(\Delta\omega_L/\omega)/(\Delta\omega_2/\omega)|$ up to $L = 50$ in Eq. (3.21) are shown in Fig. 3.9 for several representative cases. Clearly, the leading contribution is due to the lowest-order deformation (i.e., the $L = 2$ term).

As proposed in Chap. 2, droplet deformation due to a single photon can occur if fluids with low interfacial tensions are used. The WGM frequency shifts induced by the interface deformation as a result of WGM with single-photon energy ($\hbar\omega$) are shown in Fig. 3.10. Terms up to $L = 200$ are considered in the summation (3.21). The results for a lower interfacial tension assumption ($\sigma = 1\,\mathrm{mN/m}$) are also shown in the same plot. The solid lines in Fig. 3.10 correspond to the exact solutions given by Eq. (3.21), whereas the dashed lines are based on the approximate solutions in Chap. 2. The frequency shifts given by the exact solution are actually larger than our original estimates given in Chap. 2. Experimentally,

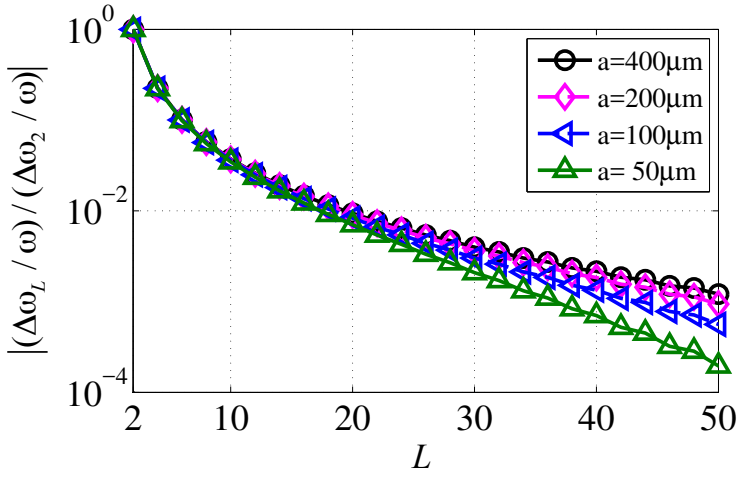

Figure 3.9: Contribution to WGM frequency shift as a result of different Y_{LM} terms in shape deformation $\Delta\omega_L/\omega$ in Eq. (3.21), normalized by the leading contribution $\Delta\omega_2/\omega$.

frequency shift as small as $\Delta\omega/\omega \sim 10^{-8}$ has been measured [85]. Based on this value and the results shown in Fig. 3.10, it should be feasible to detect the frequency shift induced by a single photon if the droplet diameter is around $10\,\mu$m and the interfacial tension is of the order of $\sigma = 1\,$mN/m. Again, our results confirm the possibility of optical nonlinearity induced by only a few photons.

It is worth mentioning that droplets with low interfacial tensions ($\sigma \leq 1\,$mN/m) have been obtained in different studies [86, 68, 45]. With the help of surfactant, an interfacial tension as low as $1\,\mu$N/m was obtained in an emulsion system [67].

To investigate the nonlinear optofluidic effects for higher order WGMs $|l, m\rangle$ with $m < l$, we also calculate the droplet interface deformations and the frequency changes induced by such modes. The results are shown in Fig. 3.11 as blue (dark gray) bars, which give the frequency shifts of the $|l, m\rangle$ mode. For these results, the radiation pressure is produced by the $|l, m\rangle$ mode itself. Note that the fundamental mode $|l, l\rangle$ generates the largest frequency shift. Since the droplet is no longer a sphere, the $(2l + 1)$-fold degeneracy of the WGM should be broken. To quantify this effect, we also calculate the frequency shifts of the $|l, m\rangle$ mode, where the radiation pressure is produced by the fundamental WGM mode $|l, l\rangle$. The results are again shown in Fig. 3.11 as red (light gray) bars. As expected, WGMs with the same l but different m numbers are no longer degenerate. All results in Fig. 3.11 are based on a droplet with radius $a = 100\,\mu$m, with $l = 1275$ and $P_{\mathrm{WGM}} = 1\,$W for the WGMs.

In the calculation of the thermal effects, we neglected the thermocapillary effect caused by the temperature increase. To justify this, here we estimate the interfacial tension increase and the resulting shear stress on the interface. Based on the well-known Eötvös rule [87], the interfacial tension of the fluid system is given by $\sigma = \bar{k}(T_c - T)/\bar{V}^{2/3}$, where $\bar{k}$ and $\bar{V}$ are material properties and T_c is the critical temperature of the fluid. Using the critical

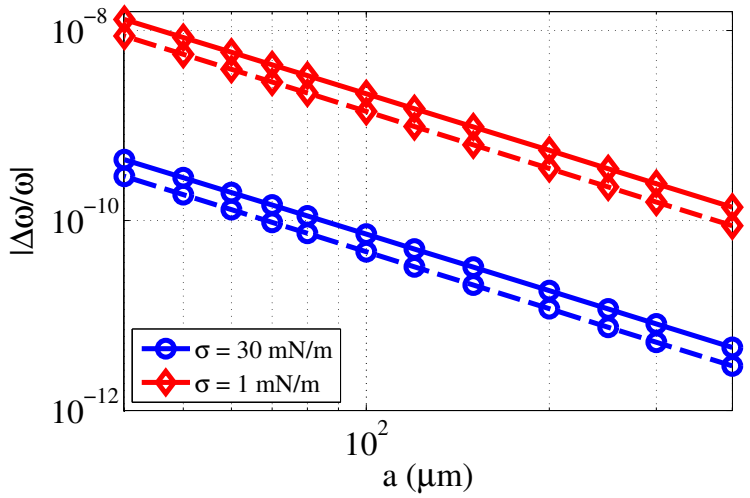

Figure 3.10: WGM frequency shift induced by the radiation pressure of a single photon for interfacial tension $\sigma = 30\,\mathrm{mN/m}$ and $\sigma = 1\,\mathrm{mN/m}$. Solid lines are the frequency shift values computed by the exact interface shape, while dashed lines are computed from the first-order approximated interface deformation.

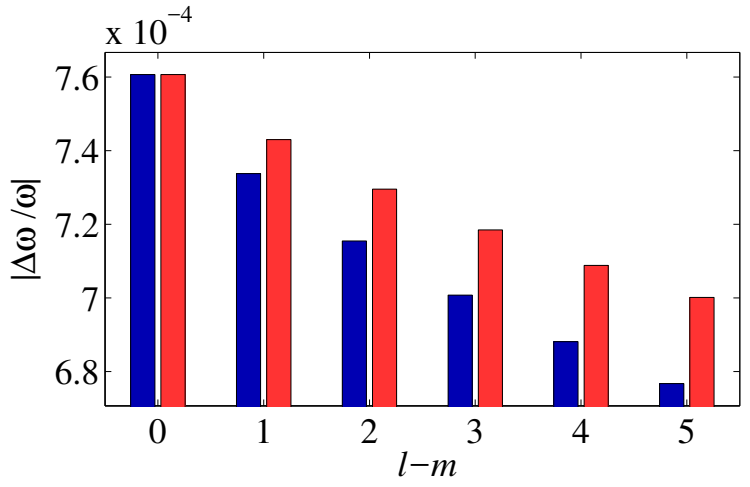

Figure 3.11: Resonance frequency shift in a droplet with radius $a = 100\,\mu\mathrm{m}$ and interfacial tension $\sigma = 30\,\mathrm{mN/m}$ for WGMs $|l, m\rangle$ with the same $l = 1275$ but different m numbers. The blue (dark gray) bars give the frequency shifts of the $|l, m\rangle$ mode that is caused by the radiation pressure of itself, i.e., the $|l, m\rangle$ mode. The red (light gray) bars are the frequency shift of the $|l, m\rangle$ mode, where radiation pressure is produced by the fundamental mode $|l, l\rangle$.

temperature of water $T_c = 374\,^{\circ}\mathrm{C}$, and a temperature increase of $1\,^{\circ}\mathrm{C}$ from room temperature ($25\,^{\circ}\mathrm{C}$), the change in interfacial tension is $\Delta\sigma/\sigma = -0.28\%$. Along the arc length of the droplet interface, s, the shear stress is roughly, $\partial\sigma/\partial s \approx 1.8 \times 10^{-3}(\sigma/a)$. Compared with the maximum radiation pressure on the interface of the $a = 100\,\mu\mathrm{m}$ droplet, $p_{\mathrm{opt}}^{\mathrm{max}} \approx 6 \times 10^{-2}(\sigma/a)$, we have $(\partial\sigma/\partial s)/p_{\mathrm{opt}}^{\mathrm{max}} \approx 3\%$. Thus, the thermocapillary effect can be neglected in our calculations of the interface deformation.

Our calculations on droplets with lower surface tension show that a single photon can possibly produce measurable interfacial deformation. However, recent studies show that the effect of thermal fluctuations may become important for interfaces with low interfacial tension [88, 89], and thus it might be difficult to distinguish the single photon effect from those due to thermal fluctuations. To reduce the effect of thermal fluctuation experimentally, we may consider using liquid drops at low temperature. For example, the surface tension of a liquid helium droplet at temperature $T < 1\,\mathrm{K}$ is $\sigma \sim 0.38\,\mathrm{mN/m}$ [90], which is low enough to admit single-photon nonlinearity.

In summary, this section confirms the feasibility of single-photon-level nonlinearity if the interfacial tension of the liquid droplet is of the order of $\sigma = 1\,\mathrm{mN/m}$ or less. Our results also suggest that radiation-pressure-induced deformation should lift the degeneracy of the WGMs.

3.7 Conclusion

In this chapter, we investigate the nonlinear optofluidic effect in microsized liquid resonators. The nonlinearity is induced by the radiation pressure associated with a high-Q WGM. The interface deformation of the liquid droplet is calculated both analytically by force balance and numerically by BEM, which agree with each other very well. The effect of temperature change is also quantified by BEM. The nonlinearity induced by the radiation pressure is shown to be higher than the temperature effect and the Kerr effect. Based on our analytical and numerical models, we confirm the possibility of measurable optofluidic nonlinearity at the single-photon energy level. The conditions that may allow one to experimentally observe single-photon-level nonlinear optofluidic effects are also discussed. Experimental measurement of the nonlinearity induced by the radiation pressure will be performed using the white light interferometry technique for future research.

Chapter 4

Comparative analysis of nonlinear optofluidic processes in microdroplets

4.1 Abstract

Our prior work has shown that high quality (Q) factor whispering gallery modes (WGMs) in liquid microdroplets can potentially induce single-photon-level nonlinear effects through radiation pressure on the interface. However, little is known about the nonlinear effects of other processes involving scattering force and thermocapillarity. In this study, we establish a numerical framework that can calculate the fluid motion and the resultant nonlinearity induced by the optical scattering force and thermocapillarity. Then, we compare the magnitude of various nonlinear optofluidic processes induced by the radiation pressure, the thermocapillary effect, the scattering-induced optical force and the Kerr effect. Using realistic fluid parameters, we show that the radiation pressure due to the WGM produces the strongest nonlinear optofluidic effect.

4.2 Introduction

Optofluidics was originally developed for important applications such as lasing [51], sensing [29, 52], and display [6, 91, 48]. The mechanical interplay between light and liquid, however, has not been thoroughly investigated, even though the first demonstration of liquid motion actuated by a focused laser beam was reported as early as 1973 [2]. Since the classic work by Ashkin and Dziedzic, the distortion of a liquid system induced by a high intensity laser beam has been studied in [59, 8, 9, 6, 61, 76, 5, 13, 10, 11], where both flat and spherical fluid interfaces were considered.

In Chaps. 2&3 and Ref. [78, 92], we analyzed a highly nonlinear optofluidic system that is

comprised of light circulating in a liquid droplet in the form of a high quality (Q) factor whispering gallery mode (WGM). In such a system, the radiation pressure of the high-Q WGM can push the droplet surface outwards and form the bulge depicted in Fig. 1. Perhaps the most interesting result of our theoretical analysis is that the strength of the radiation pressure induced nonlinearity exceeds that of the Kerr nonlinearity by up to six orders of magnitude. As a result, the radiation pressure induced nonlinear optofluidics may ultimately produce nonlinear effects at single photon energy level. Our prior work only considered nonlinear effects due to radiation pressure. Yet besides radiation pressure, optical fields can also actuate fluid motions through scattering force [5] and thermocapillary force [14]. In this paper, we compare the magnitude of nonlinear effects induced by the scattering force and the thermocapillary force, as well as radiation pressure induced nonlinearity and other nonlinear effects.

When light is elastically scattered by inhomogeneities in the fluid (e.g., suspended particles or density fluctuations), the light momentum can be changed, which results in a scattering force that may induce fluid motion in the volume. For example, a cylindrical dripping liquid jet was produced by light scattering in a microemulsion and the dripping rate was theoretically predicted [93]. The fluid motion due to the light scattering was also observed in a fluid layer with a flat interface [12], where a toroidal fluid recirculation was produced by a vertically incident laser beam. The scattering force induced an interface deformation that was found to be on the same order of magnitude as the deformation induced by the radiation pressure. The effects of light scattering in a similar setup were simulated numerically by the boundary element method in [13], which showed good agreement with experimental observations. In these studies, the scattering force in the fluid has been modeled as a body force that depends on the light intensity. Similarly, in the case of WGMs circulating in a liquid droplet, the effect of light scattering should also produce a body force in liquid resonators in the same direction of the WGM propagation. For experimental studies of nonlinear effects in microdroplets, it is highly relevant to theoretically estimate the magnitude of interfacial deformation due to the scattering force.

Another potentially relevant factor is the thermocapillary force. The localized light heating in the liquid may result in a temperature gradient, which leads to thermocapillary stresses on the fluid interface. The thermocapillary effect of laser heating has been applied in drop sorting, merging and microfluidic valve [14, 94, 95], etc. Baroud et al. [14] demonstrated that the thermocapillary force could induce a circulation of fluid in a droplet and thus control the motion of the droplet. In our work on microdroplets as whispering gallery resonators (Chap. 3), we computed the temperature increase due to the WGM energy absorption, from which the volume expansion and refractive index change were estimated. Since the temperature varies along the fluid interface, the thermocapillary effect may arise and induce interfacial flow on the droplets. Such effect can therefore lead to another class of nonlinear optofluidic processes, which was not analyzed quantitatively in the previous calculations (Chap. 3).

The objective of this work is to develop a boundary element model to evaluate the nonlinear

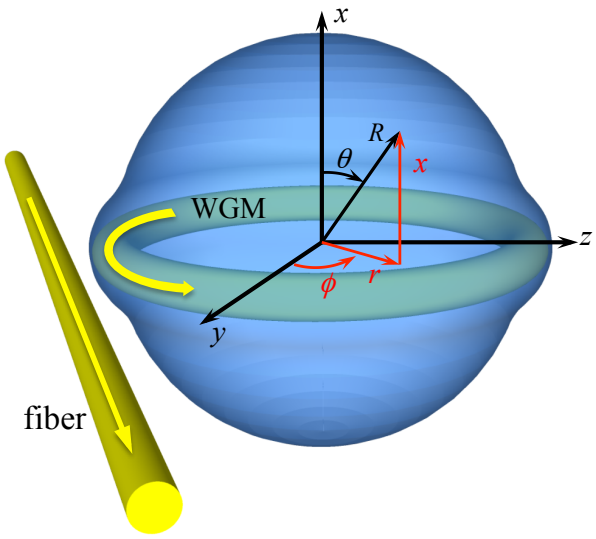

Figure 4.1: Schematics of a high-Q WGM circulating along the equator of a droplet induced by the laser in a nearby fiber. The yellow arrows indicate light propagation directions. A cylindrical coordinate (x, r, ϕ) and a spherical coordinate (R, θ, ϕ) are defined to assist further analysis.

optofluidic effects induced by the light scattering and the thermocapillary force associated with the WGMs in microdroplets. We quantify the magnitudes of these two nonlinear processes, and compare them with nonlinearities induced by the radiation pressure as well as the thermal and Kerr effects. Specifically, in Sect. 4.3, the boundary element formulations for Stokes equations with scattering force and thermocapillary force are derived in an axisymmetric domain. The fluid motion induced by various optofluidic processes are analyzed and compared in Sect. 4.4. The nonlinearities associated with the interfacial deformation are also compared with purely thermal effects such as volume expansion and refractive index changes induced by temperature changes, as well as the Kerr nonlinearity.

4.3 Optical field induced fluid motion

We consider a system of a high-index liquid micro-droplet (core) immersed in a low-index immiscible fluid (cladding). Such a system can support a high-Q WGM circulating along the equator of the droplet, as illustrated in Fig. 4.1. By assuming a transverse electric (TE) mode, the optical field in the resonator has been calculated analytically in [19, 78], the derivations of which will not be repeated here. In this paper, we denote variables associated with the core phase with subscript "co" and the cladding phase with subscript "cl".

In this section, we derive boundary element models to quantitatively calculate the fluid

motion actuated by the scattering force, thermocapillary force and radiation pressure induced by the WGM in the droplet.

4.3.1 Effect of light scattering

Due to the fluid inhomogeneity, the optical field in the droplet may induce a scattering force in the same direction as the light propagation [93, 13],

$$\boldsymbol{F} = \varpi \frac{n_{co}}{c} S_\phi \boldsymbol{e}_\phi, \tag{4.1}$$

where ϖ is the forward light momentum attenuation coefficient (or turbidity), n_{co} is the refractive index of the core phase, c is the speed of light and S_ϕ is the ϕ component of the Poynting vector, which represents the light intensity. Note that S_ϕ (and thus $\boldsymbol{F}$) is independent of ϕ. Due to its direction, the scattering force $\boldsymbol{F}$ may cause a circulation motion of the fluid. With known force magnitude, it is possible to compute the fluid velocity numerically.

The motions of the fluid interface and volume are governed by the Navier-Stokes equations. For a typical drop with radius $a \sim 100\,\mu$m, characteristic velocity $U \sim 10^{-3}\,$m/s, density difference $\rho \sim 200\,\mathrm{kg/m^3}$ and fluid viscosity $\mu \sim 13\,\mathrm{mPa \cdot s}$, the Reynolds number is approximately $Re = \rho U a/\mu \sim 10^{-2}$. As a consequence of the low Reynolds number, the Stokes assumption is valid for our system. In the presence of the scattering force, the Stokes equations and incompressibility condition can be written as,

$$-\nabla p_d + \mu \nabla^2 \boldsymbol{u} + \boldsymbol{F} = 0, \nabla \cdot \boldsymbol{u} = 0, \tag{4.2}$$

where the dynamic pressure p_d is defined as the sum of actual fluid pressure and centrifugal effect of the fluid motion $p_d = p + \rho u_\phi^2/2$.

The Boundary Element Method (BEM) has been widely used to solve the stokes equations numerically [96, 79, 41]. For a two-phase fluid system with a sharp interface in the three-dimensional domain, the interfacial velocity and pressure are related by the following boundary integral equations (BIE),

$$\begin{aligned} u_j(\boldsymbol{x}_0) = {} & b_1 \int_S G_{ji}(\boldsymbol{x}_0, \boldsymbol{x}) f_i(\boldsymbol{x})\, dS(\boldsymbol{x}) \\ & + b_2 \int_S u_i(\boldsymbol{x}) K_{ijm}(\boldsymbol{x}_0, \boldsymbol{x}) n_m(\boldsymbol{x})\, dS(\boldsymbol{x}) \\ & + b_1 \int_V G_{ji}(\boldsymbol{x}_0, \boldsymbol{x}) F_i(\boldsymbol{x})\, dV(\boldsymbol{x}), \end{aligned} \tag{4.3}$$

where $b_1 = -1/(4\pi\mu_{cl}(1+\lambda))$, $b_2 = (1-\lambda)/(4\pi(1+\lambda))$, $\lambda = \mu_{co}/\mu_{cl}$ is the viscosity ratio of the core and cladding phases; $\boldsymbol{f}$ is the total stress on the interface; "S" denotes the interface

of the droplet; position vectors $\boldsymbol{x}$ and $\boldsymbol{x}_0$ are located on the fluid interface. Indices i, j, m take values of $1, 2, 3$ and repeated indices are summed. The Green's functions G_{ij} and K_{ijm} for Stokes flow in free space take the form,

$$G_{ij}(\boldsymbol{x}, \boldsymbol{y}) = \frac{1}{s}\delta_{ij} + \frac{1}{s^3}s_i s_j,\ K_{ijm}(\boldsymbol{x}, \boldsymbol{y}) = -\frac{6}{s^5}s_i s_j s_m, \tag{4.4}$$

with $s_i = x_i - y_i$, $s = |\boldsymbol{s}|$, and δ_{ij} is the identity tensor.

Due to the axial symmetry of the droplet geometry, boundary conditions, as well as the WGM-induced scattering force, all the velocity and force variables in Eq. (4.3) should be independent of the coordinate ϕ. Therefore, we can integrate Eq. (4.3) over the ϕ direction analytically to lower the dimension of numerical discretization and integration. We can show that the integration over ϕ direction results in the decomposition of Eq. (4.3) into the following x-r and ϕ components,

$$\begin{aligned} u_\alpha(\boldsymbol{x}_0) &= b_1 \int_C M_{\alpha\beta}(\boldsymbol{x}_0, \boldsymbol{x}) f_\beta(\boldsymbol{x}) dl(\boldsymbol{x}) \\ &\quad + b_2 \int_C Q_{\alpha\beta\gamma}(\boldsymbol{x}_0, \boldsymbol{x}) u_\beta(\boldsymbol{x}) n_\gamma(\boldsymbol{x}) dl(\boldsymbol{x}), \end{aligned} \tag{4.5a}$$

$$\begin{aligned} u_\phi(\boldsymbol{x}_0) &= b_2 \int_C u_\phi(\boldsymbol{x}) Q_{\phi\phi\gamma}(\boldsymbol{x}_0, \boldsymbol{x}) n_\gamma(\boldsymbol{x}) dl(\boldsymbol{x}) \\ &\quad + b_1 \int_A F_\phi(\boldsymbol{x}) M_{\phi\phi}(\boldsymbol{x}_0, \boldsymbol{x}) dA(\boldsymbol{x}). \end{aligned} \tag{4.5b}$$

In Eq. (4.5), indices α, β, γ take the value of 1 and 2, representing the x- and r-directions, respectively. "C" and "A" represent the interface and the volume of the fluid domain intercepted with a ϕ = constant plane. Note that Eq. (4.5a) is the same as the BIE in axisymmetric domain with no ϕ component of velocity or force derived in literature [79], whereas Eq. (4.5b) is the new BIE that governs the swirling motion of the fluid induced by the azimuthal component of the scattering force. As shown by Eq. (4.5), the ϕ component of the velocity field is decoupled from u_x and u_r. However, the centrifugal effect of u_ϕ can produce an interface force that subsequently induces fluid motion in x- and r-directions. This is evidenced by the expression of the total force on the interface,

$$\boldsymbol{f} = (2\sigma\kappa_m - \Delta\rho u_\phi^2/2)\boldsymbol{n}, \tag{4.6}$$

where κ_m is the mean curvature of the interface. The detailed derivations of Eq. (4.5) are shown in Appendix C.

In our simulations, the fluid interface on the ϕ = constant plane is discretized into N circular arc elements, and $\boldsymbol{x}_0$ is located at the center of each element. On each element, the surface velocity and pressure are assumed to be constant, and the axisymmetric Green's functions are integrated numerically using Gauss Quadrature. Note that Green's functions may exhibit logarithmic singularities as $\boldsymbol{x} \to \boldsymbol{x}_0$, and special treatment is need to ensure the accuracy

of numerical integration. The detailed derivations of the singularity behaviors and their numerical integration schemes are shown in Appendix D.

Equation (4.5) can then be discretized and written as linear systems relating the unknown interface velocity vector ($\{v^{xr}\}, \{v^{\phi}\}$) with the interface force vector ($\{f\}$) or the volume force integral ($\{I^F\}$),

$$[A]\{v^{xr}\} = [B]\{f\}, \tag{4.7a}$$

$$[H]\{v^{\phi}\} = \{I_i^F\}, \tag{4.7b}$$

where $[A]$, $[B]$ and $[H]$ are matrices whose entries are related to the integrals of $M_{\alpha\beta}$ and $Q_{\alpha\beta\gamma}n_\gamma$ on the interface elements.

In the simulation, the linear system Eq. (4.7b) is solved first and the u_ϕ distribution is obtained. The total interface force including the centrifugal effect of u_ϕ is then computed and used in Eq. (4.7a), the solution to which results in the velocity components within the ϕ =constant plane. The solution to the above linear systems gives the velocity at the center of each element on the interface. Velocity values at the end points of each element are interpolated by a cubic spline with vanishing derivatives at $x = \pm a$. The element edges and center displacements are integrated over a time step Δt by the explicit Euler scheme, i.e., $\Delta \boldsymbol{x} = \boldsymbol{u}\Delta t$, and a new interface shape is produced for the following time step. At each time step, a new linear system Eq. (4.7) is generated based on the updated interface shape. The time step size is chosen by the criteria $\Delta t \leq \tau_m = (\mu_{co} + \mu_{cl})\delta/(2\sigma)$, where δ is the element size [39]. This process is iterated until the maximum velocity magnitude $|\boldsymbol{u}|$ is 1000 times smaller than the initial velocity magnitude. In our simulations, we find that $N = 128$ elements can provide results with adequate accuracy.

4.3.2 Thermocapillary effect

As shown in Chap. 3, the absorption of the WGM energy by the droplet may result in the temperature change in the fluid, which leads to changes in the droplet volume and the refractive index. In addition, the temperature gradient on the fluid interface can also induce the thermocapillary effect, i.e., a shear stress along the interface. Using the well-known Eötvös rule [87], the interfacial tension of the fluid system at a given temperature T is,

$$\sigma_T = \bar{k}\bar{V}^{-2/3}(T_c - T), \tag{4.8}$$

where $\bar{k}$ and $\bar{V}$ are material properties and T_c is the critical temperature of the fluid. Assuming that the interfacial tension at room temperature T_0 is σ, the value of σ_T can then be derived as,

$$\sigma_T = \sigma\frac{T_c - T}{T_c - T_0}. \tag{4.9}$$

With known temperature distribution on the fluid interface, the gradient of the interfacial tension, $\partial\sigma_T/\partial s$, can be calculated and the total stress on the interface is,

$$\boldsymbol{f} = (2\sigma\kappa_m)\boldsymbol{n} - (\partial\sigma_T/\partial s)\boldsymbol{t}. \tag{4.10}$$

The fluid velocity induced by the thermocapillary effect can then be computed by Eqs. (4.5a) and (4.7a).

Note that as modeled in Chap. 3, the fluid motion induced by the optical radiation pressure, $p_{\text{opt}} = \frac{1}{2}\epsilon_0 (n_{co}^2 - n_{cl}^2) |\boldsymbol{E}_{\text{surf}}|^2$ [8, 78], is also governed by Eqs. (4.5a) and (4.7a) with the total stress on the interface $\boldsymbol{f} = (2\sigma\kappa_m - p_{\text{opt}})\boldsymbol{n}$.

So far, we have developed BEM models that can simulate the fluid motion and interface dynamics of the droplets under scattering force, thermocapillary and radiation pressure effects. In the following section, the fluid motion and the interface deformation induced by the aforementioned nonlinear optofluidic processes will be computed and their magnitudes will be compared.

4.4 WGM induced nonlinearities in Liquid Droplets

In this study, we choose a liquid system based on an oil droplet immersed in water, which has the same properties as the system analyzed in Chap. 3. Fluid viscosities of the core and cladding media are $\mu_{co} = 13\,\text{mPa}\cdot\text{s}$ and $\mu_{cl} = 1\,\text{mPa}\cdot\text{s}$. The forward light momentum attenuation coefficient of the core fluid is assumed to be $\varpi = 70\,\text{m}^{-1}$. (For a transparent liquid with low attenuation, such as an index matching fluid, the value of $\varpi = 70\,\text{m}^{-1}$ is likely an overestimate. However, as will be shown later, a more accurate estimate for ϖ is unnecessary.) The oil-water interfacial tension at room temperature is $\sigma = 30\,\text{mPa}\cdot\text{s}$. The properties of the WGMs depend on the liquid refractive indices as well as the geometry of the resonator. This liquid droplet can possess high-Q factor in the visible wavelength range. For simplicity, we choose the WGM wavelength to be $\lambda \approx 700\,\text{nm}$, with the effective refractive indices of the core and cladding phases $n_{co} = 1.44$ and $n_{cl} = 1.33$, respectively. The mode numbers and resonance wavelengths of the fundamental WGMs $|l, l\rangle$ are provided by [92] and shown in Table 4.1. The electric field $\boldsymbol{E}$ and the Poynting vector ϕ-component (S_ϕ) distribution are computed following the formula provided in Chap. 3. The circulating WGM power is assumed to be 1 W for all calculations in this work.

In this section, the fluid motion in the droplet as a result of the radiation pressure, light scattering and thermocapillarity are calculated following the numerical procedure described in Sect. 4.3. The optofluidic nonlinearities due to the interface deformation are computed and compared.

Table 4.1: Angular Mode Number l and Resonance Wavelength λ of WGMs in Liquid Droplets (Chap. 3).

$a(\mu\text{m})$	400	300	250	200	150	120
l	5145	3847	3204	2569	1918	1529
λ(nm)	699.35	700.66	700.45	698.05	699.95	701.26
$a(\mu\text{m})$	100	80	70	60	50	40
l	1275	1018	889	761	632	504
λ(nm)	699.75	699.65	700.05	699.75	700.55	700.59

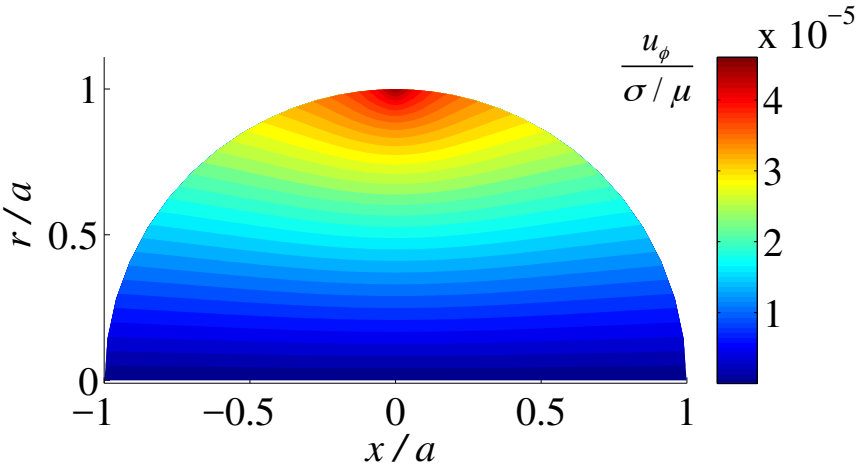

Figure 4.2: Velocity u_ϕ component distribution induced by light scattering in the volume of the $a = 100\,\mu$m droplet on a $\phi =$ constant plane.

4.4.1 WGM induced Fluid Motion

We first look at the fluid motion due to the light scattering force Eq. (4.1) in the volume of the droplet. The rotational velocity (u_ϕ) of the droplet is shown in Fig. 4.2. The rotational motion of the droplet leads to an centrifugal force on the interface, which results in a velocity field on the x-r plane. This velocity field at $t = 0$ is shown in Fig. 4.4(a).

The fluid motion induced by the radiation pressure has been studied in Chap. 3, which is also shown in Fig. 4.4(b). To calculate the thermocapillary effect, the temperature distribution on the droplet interface is also computed by the BEM. The detailed BEM formulations are available in Chap. 3 and the temperature increase on the droplet interface is shown in Fig. 4.3. With the shear stress due to the interfacial tension gradient given by Eqs. (4.9) and (4.10), the fluid motion in the droplet can be produced by the BIE (4.5a), which is shown in Fig. 4.4(c). As evidenced in Fig. 4.4, the velocity field in the x-r plane due to the droplet

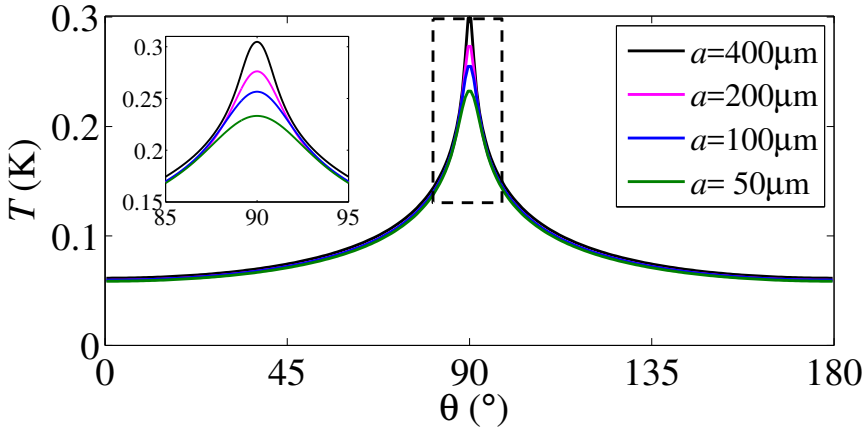

Figure 4.3: Variation of temperature on the interface of droplets with radii $a = 50, 100, 200, 400\,\mu$m as a result of thermal heating.

rotation is several orders of magnitude smaller than the velocity induced by the radiation pressure and thermocapillarity.

The droplet interface deforms under nonzero u_x and u_r distribution on the interface. The interface forces under the effect of centrifugal force and radiation pressure are eventually balanced by the surface tension force resulting from the interface deformation. On the other hand, the shear stress due to thermocapillarity would still actuate fluid motion on a balanced droplet. The velocity filed in a balanced droplet due to thermocapillarity is shown in Fig. 4.5. Similar to the fluid motion reported in other systems [14], Fig. 4.5 shows that fluid circulations are also present in our system.

Under the velocity field shown in Fig. 4.4, the balanced interface shape can be obtained by time integration of the interface position until the normal component of the interface velocity vanishes. The droplet interface deformation for all the twelve cases shown in Table 4.1 under the effects of radiation pressure, light scattering and thermocapillarity are shown in Fig. 4.6. Since the overall shapes of the interface deformation are self-similar, when normalized by the interface displacement at $\theta = \pi/2$, each curve shown in Fig. 4.6 is in fact a collection of results for the twelve microdroplets listed in Table 4.1, each with a different radius. We also observed that the interface deformation induced by the light scattering is several orders of magnitude smaller than the radiation pressure effect. This phenomenon is different from the results reported on a flat fluid interface [13], where micron-scale deformation was induced by the scattering of a vertically incident laser beam. On a flat fluid interface, the scattering force and the radiation pressure were in parallel directions and were observed to induce the interface deformation on the same order of magnitude. However, in our system, the interface deformation is in an orthogonal direction to the scattering force and is induced indirectly by the weakly coupled centrifugal effect.

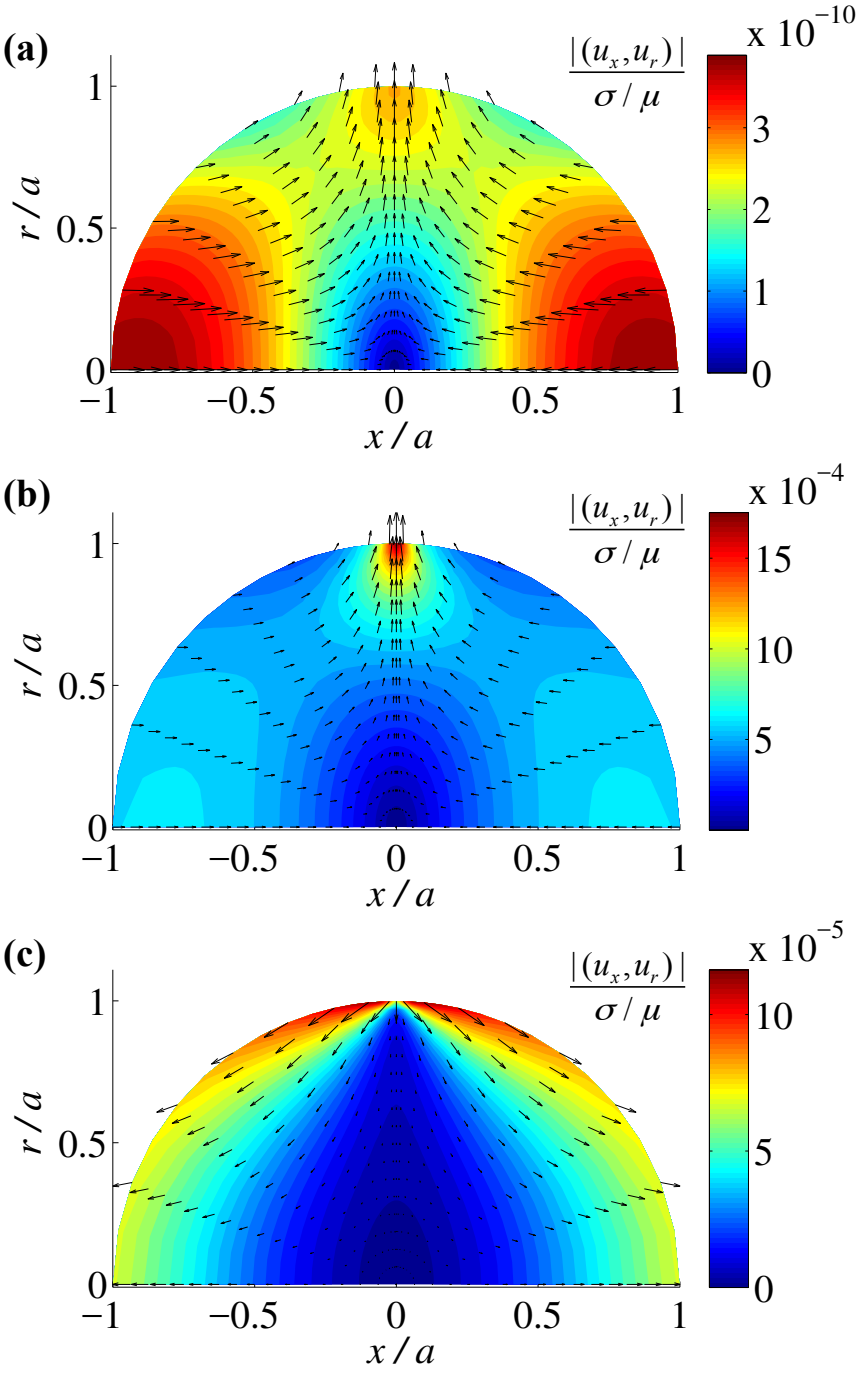

Figure 4.4: Velocity distribution in the x, r directions at $t = 0$ induced by (a) light scattering in the fluid, (b) radiation pressure and (c) thermocapillary effect on the interface of the $a = 100\,\mu$m droplet on a $\phi =$ constant plane.

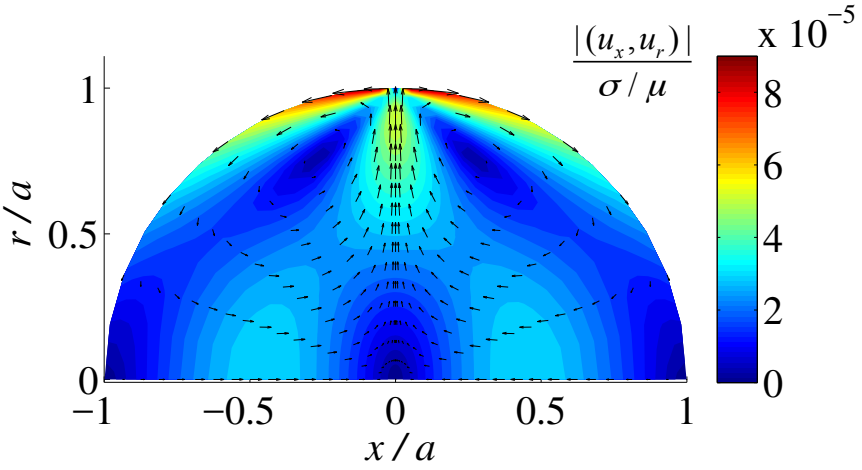

Figure 4.5: Velocity distribution as a result of the thermocapillary effect in a droplet with balanced interface shape. The radius of the droplet is $a = 100\,\mu$m.

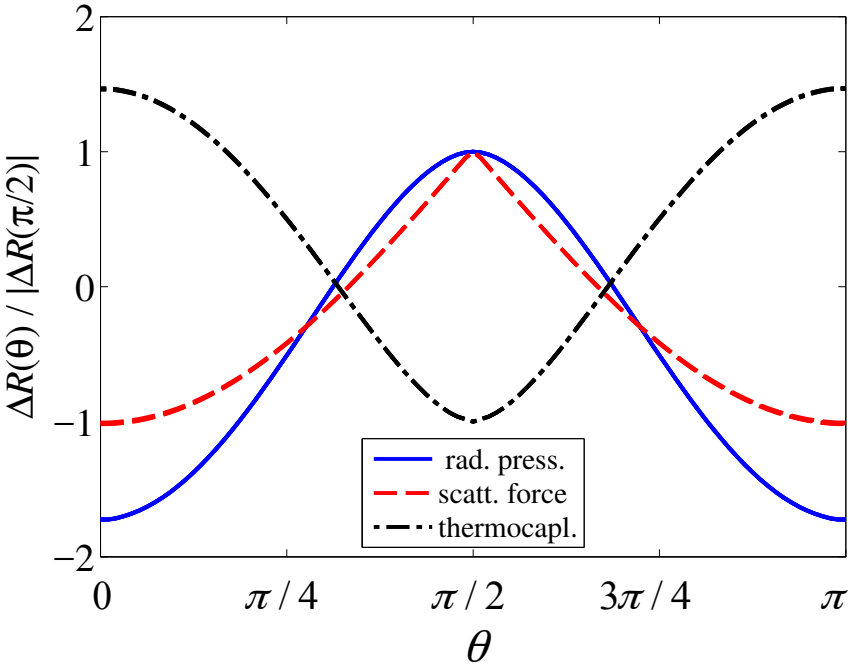

Figure 4.6: Droplet interface deformation under the effects of radiation pressure, light scattering and thermocapillarity, normalized by the interface displacement magnitude at $\theta = \pi/2$. Due to the normalization, each curve shown here is in fact a collection of twelve curves (see Table 4.1) collapsed together.

4.4.2 Optofluidic Nonlinearities

In this section, we compare the magnitude of nonlinear effects associated with the fundamental WGM $|l, l\rangle$, with the mode number l given by Table 4.1. As discussed in Chaps. 2&3, the droplet interface deformation may induce a WGM resonance frequency shift, which is similar to the Kerr effect. In addition, the increase of temperature in the droplet leads to the volume expansion as well as refractive index changes, which also result in WGM resonance frequency shifts. The refractive index change and the droplet radius expansion have been estimated in Chap. 3 as, $\Delta n_T = (dn/dT)T_{\max}$ and $\Delta R_T = \alpha_T T_{\max}/3$, respectively, where $T_{\max}$ is the maximum temperature increase in the droplet, $dn/dT = -3.9 \times 10^{-4}\,\mathrm{K}^{-1}$ is the thermal coefficient of refractive index and $\alpha_T = 8 \times 10^{-4}\,\mathrm{K}^{-1}$ is the thermal expansion coefficient of the proposed system.

Due to the Kerr effect, the refractive index of the liquid depends linearly on the optical field intensity. The maximum refractive index change can be estimated as $\Delta n \approx \chi^{(3)}|\boldsymbol{E}|^2_{\max}$, where $\chi^{(3)}$ is the third order nonlinear optical susceptibility, and $|\boldsymbol{E}|_{\max}$ is the maximum electric field intensity in the droplet. We use the susceptibilities of water and carbon disulfide (CS_2) ($\chi^{(3)}_{\mathrm{water}} = 2.5\times10^{-22}\,\mathrm{m}^2/\mathrm{V}^2$ and $\chi^{(3)}_{\mathrm{CS_2}} = 3.1\times10^{-20}\,\mathrm{m}^2/\mathrm{V}^2$) to provide an order of magnitude estimate of the Kerr effect.

We now compare the magnitude of various nonlinear processes due to the radiation pressure, temperature induced droplet expansion and index change, thermocapillary force, Kerr effect and optical scattering force in liquid droplets. Let us define the interface deformation at the equator ($\Delta R(\theta = \pi/2)/a$) under radiation pressure, thermocapillary and light scattering effects as ΔR_{rad}, ΔR_{cap} and ΔR_{scatt}, respectively. As shown in Fig. 4.7, interface deformation induced by the radiation pressure (ΔR_{rad}) is higher than other nonlinear effects. Additionally, nonlinearities associated with the thermocapillarity, volume expansion and index change due to the temperature increase are also much stronger than the Kerr effect. The interface deformation induced by the light scattering, on the other hand, is smaller than the Kerr effect and thus should not play significant roles in droplets with diameter less than 1 mm. Finally, we point out that in order to support high-Q WGMs, the liquid that forms the microdroplet must possess low attenuation, which means that the value for ϖ should not exceed $100\,\mathrm{m}^{-1}$. Therefore, for sub-mm-scale droplets that support high-Q WGMs, the nonlinearity induced by the scattering force can be safely ignored.

4.5 Conclusion

In this paper, we develop boundary element models to calculate the fluid motion and droplet deformation due to the scattering force and thermocapillary force produced by a high-Q WGM in liquid droplets. The BIEs are derived in an axisymmetric domain that incorporate the effect of radiation pressure, scattering force and thermocapillary effect. We show that the

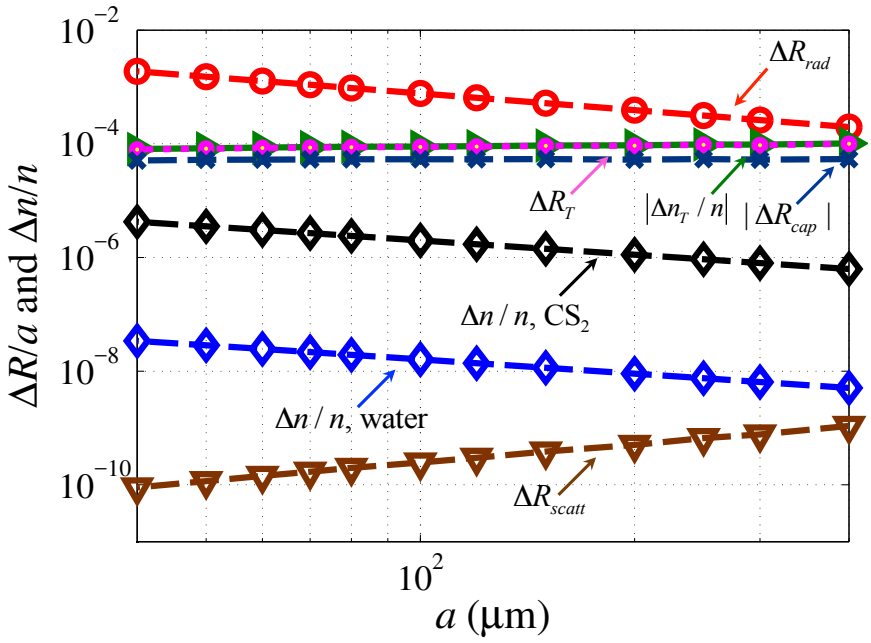

Figure 4.7: Comparison of nonlinearities associated the the radiation pressure, thermal effects, Kerr effect and light scattering. The power of the WGM in the droplet is assumed to be 1 W.

radiation pressure on the droplet interface should induce the highest velocity magnitude and the largest interface deformation, and thus lead to the strongest nonlinearity compared to the thermal effects, Kerr effect and light scattering. Due to the weakness of the centrifugal effect, the scattering force nonlinearity is several orders of magnitude smaller than the Kerr effect and thus can be safely neglected. The results presented here can guide future experimental studies of WGM-induced nonlinear optofluidic processes in liquid droplets.

Chapter 5

Discussion and Conclusions

5.1 Overview of study

In this dissertation, different optofluidic effects of the light whispering gallery mode (WGM) in liquid resonators are studied and compared. The system is assumed to consist of a liquid droplet resonator immersed in water. The resonator has the properties of an index matching fluid, whose refractive index is higher than that of water. For a given resonator radius and light wavelength, the electromagnetic field of the WGM inside the droplet is calculated, from which the radiation pressure can be analytically determined.

We first provide an approximated solution of the radiation pressure induced droplet interface deformation. The deformed interface of the droplet is assumed to maintain a spheroid shape, which can be described by a single parameter – the major axis length. According to the Young-Laplace equation, the radiation pressure should be balanced by the interfacial tension on the balanced interface. The force balance equation is solved by a spherical harmonic integration and the droplet interface deformation is expressed as a function of the WGM power. Systems with various experimentally attainable properties are investigated.

In order to obtain a more accurate estimation of the radiation effect, the exact solution of the droplet deformed interface is also provided. The exact interface deformation can be obtained in two different ways. We first solve for the unknown interface shape by the linearized Young-Laplace equation. Then the dynamic response of the interface under the radiation pressure is simulated numerically by the boundary element method (BEM). The thermal expansion and thermal refractive index change can be calculated from the temperature field in the droplet, which is also solved by BEM. The nonlinearities induced by the radiation pressure and laser heating are compared with the Kerr effect.

The effect of light scattering and thermocapillarity are then quantified for the same system. Since the scattering force acts along the light propagation direction, the axisymmetric BEM

needs to be modified to account for the azimuthal body force component. The interface deformation caused by the centrifugal effect of the drop rotation is also estimated. With known Marangoni shear stress on the interface, the fluid circulation in the droplet is also produced by BEM.

5.2 Summary of results

From the approximated calculations of the spherical liquid droplet interface deformation, we find that with sufficiently high power, the optical force associated with the circulating WGM can deform the liquid droplet and induce a frequency shift of the WGM resonance. By applying spherical harmonic expansion, we estimate that the radiation pressure induced nonlinearity is several orders of magnitude stronger than the traditional Kerr effect. In fact, we find that by using a liquid system with low but experimentally achievable surface tension, it is possible to produce measurable frequency shift at the energy level of a few photons. Such effects may ultimately lead to nonlinear interactions between two single photons.

The exact calculations of the droplet deformation and temperature increase in the fluid show that the nonlinearity induced by the radiation pressure is stronger than the temperature effect and Kerr effect. Based on our analytical and numerical models, we confirm the possibility of measurable optofluidic nonlinearity at single photon energy level. The conditions that may allow one to experimentally observe single photon level nonlinear optofluidic effects are also discussed. Experimental measurement of the nonlinearity induced by the radiation pressure can be performed using the white light interferometry technique for future research.

A new boundary integral equation is derived in an axisymmetric domain that incorporates the effects of radiation pressure, scattering force and thermocapillarity. We show that the radiation pressure on the droplet interface can induce the highest velocity magnitude and the largest interface deformation, and thus lead to the strongest nonlinearity compared to the thermal effects, Kerr effect and light scattering. Due to the weakness of the centrifugal effect, the scattering force nonlinearity is several orders of magnitude smaller than the Kerr effect and thus can be neglected.

5.3 Discussion

Our investigations of the radiation pressure, scattering force and thermocapillarity on a spherical liquid resonator show that the radiation pressure leads to the strongest nonlinearity. The deformation induced by the radiation pressure may ultimately lead to single photon nonlinear optical devices. Though the effects of thermocapillarity and light scattering are relatively low in this system, such effects can be enhanced if fluid systems with attainable properties are employed.

The present work focuses on analytical and numerical investigations of the optofluidic behaviors of the WGM in a liquid resonator. The resonator interface deformation and temperature field shown in this dissertation are based on the steady state of the system rather than the dynamic responses. We investigate the interaction between the WGM and fluid dynamics in our system.

5.4 Future work

Based on the conclusions as well as the limitations of this dissertation, the following topics are suggested as future work:

1. It is necessary to experimentally verify the analytical and numerical results shown in the present work. A few challenges are expected in the experiments. First, the droplet system needs to be supported and stabilized. The mechanical vibrations of the setup may lead to noise in the measurement. In terms of the temperature field measurement, the size of the thermal sensor needs to be sufficiently small in order not to interfere with the WGM. Sub-micron and nano-scale distance measurement techniques are required to resolve the interface deformation.

2. The dynamic responses of the system, including the interface vibration and temperature variation, is another interesting topic to investigate. The different time scales associated with the two can be used as a way to distinguish them experimentally.

3. Though our analyses predicts the interaction between the WGM and fluid dynamics, the geometric change in the spherical resonators are not included in the calculations of the WGM. A simulation that employs two-way coupling between the electromagnetic field and fluid dynamics is a more accurate way to predict the system responses. In this case, finite element analysis can be used to update the WGM in non-spherical resonators and adaptive meshes are sufficient to resolve the interface of the droplet.

4. As mentioned in Chaps. 2&3, the radiation pressure effect can be magnified on systems with lower interfacial tension. The effect of only a few photons may be detectable in such systems. To prove that this systems are feasible in different applications, experimental realization of the nonlinearity measurement is critical. The challenge is that with lower interfacial tension, it is more difficult to stabilize the droplet.

5. Thermal fluctuations may be another factor that influences the measurement of interface deformation. Such effects can be quantified on systems without WGMs. If the magnitude of the thermal fluctuation is comparable to the optical nonlinearity of the system, the experiment needs to be conducted in low temperature environment.

6. Finally, the analyses in this dissertation are applicable not only to spherical resonators. Systems with different geometry, i.e. flat interface, etc. also have wide applications. The analytical framework can be modified for such systems. For example, the radiation pressure has the capability of thin fluid film manipulations, which can be predicted numerically by BEM.

Chapter 6

List of Publications

A list of publications and manuscripts related to this dissertation is shown below.

- Peng Zhang, Sunghwan Jung, Aram Lee, and Yong Xu. Radiation-pressure-induced nonlinearity in microdroplets. Phys. Rev. E, 92:063033, 2015.
- Yong Xu, Peng Zhang, Sunghwan Jung, and Aram Lee. Analysis of radiation pressure induced nonlinear optofluidics. Opt. Express, 22(23):28875-28889, 2014.
- Peng Zhang, Sunghwan Jung, Aram Lee, and Yong Xu. Comparative analysis of nonlinear optofluidic processes in microdroplets. Under review.

Here is a list of other work on interfacial fluid dynamics that is not discussed in details in this dissertation:

- Peng Zhang, S. Jana, M. Giarra, P. P. Vlachos, and S. Jung. Paramecia swimming in viscous flow. The Eur. Phys. J. Special Topics, 224(17):3199-3210, 2015.
- Peng Zhang, J.M. Mines, S. Lee, and S. Jung. Particle-induced air bubble break-up in a Hele-Shaw cell. In preparation.

Bibliography

[1] John Henry Poynting. *The pressure of light*. Society for Promoting Christian Knowledge, 1910.

[2] A. Ashkin and J. M. Dziedzic. Radiation pressure on a free liquid surface. *Phys. Rev. Lett.*, 30(4):139–142, 1973.

[3] James P. Gordon. Radiation forces and momenta in dielectric media. *Phys. Rev. A*, 8:14–21, Jul 1973.

[4] Otvio Augusto Capeloto, Vitor Santaella Zanuto, Luis Carlos Malacarne, Mauro Luciano Baesso, Gustavo Vinicius Bassi Lukasievicz, Stephen Edward Bialkowski, and Nelson Guilherme Castelli Astrath. Quantitative assessment of radiation force effect at the dielectric air-liquid interface. *Sci. Rep.*, 6(20515), 2016.

[5] Jean-Pierre Delville, Matthieu Robert de Saint Vincent, Robert D. Schroll, Hamza Chrabi, Bruno Issenmann, Rgis Wunenburger, Didier Lasseux, Wendy W. Zhang, and Etienne Brasselet. Laser microfluidics: fluid actuation by light. *J. Opt. A: Pure Appl. Opt.*, 11(3):034015, 2009.

[6] Alexis Casner and Jean-Pierre Delville. Adaptative lensing driven by the radiation pressure of a continuous-wave laser wave upon a near-critical liquidliquid interface. *Opt. Lett.*, 28(18):1418–1420, 2001.

[7] R. D. Schroll, E. Brasselet, W. W. Zhang, and J. P. Delville. Bridging dielectric fluids by light: A ray optics approach. *Eur. Phys. J. E*, 26(4):405–409, 2008.

[8] H. M. Lai, P. T. Leung, K. L. Poon, and K. Young. Electrostrictive distortion of a micrometer-sized droplet by a laser pulse. *J. Opt. Soc. Am. B*, 6(12), 1989.

[9] I. Brevik and R. Kluge. Oscillations of a water droplet illuminated by a linearly polarized laser pulse. *J. Opt. Soc. Am. B*, 16(6):976–985, 1999.

[10] Simen A Ellingsen. Microdroplet oscillations during optical pulling. *Phys. Fluids*, 24(2):022002, 2012.

[11] Simen Å. Ellingsen. Theory of microdroplet and microbubble deformation by gaussian laser beam. *J. Opt. Soc. Am. B*, 30(6):1694–1710, Jun 2013.

[12] Robert Schroll, Rgis Wunenburger, Alexis Casner, Wendy Zhang, and Jean-Pierre Delville. Liquid transport due to light scattering. *Phys. Rev. Lett.*, 98(13), 2007.

[13] Hamza Chraibi, Régis Wunenburger, Didier Lasseux, Julien Petit, and J-P Delville. Eddies and interface deformations induced by optical streaming. *J. Fluid Mech.*, 688:195–218, 2011.

[14] Charles N. Baroud, Jean-Pierre Delville, Fran çois Gallaire, and Régis Wunenburger. Thermocapillary valve for droplet production and sorting. *Phys. Rev. E*, 75:046302, Apr 2007.

[15] Roman O. Grigoriev. Chaotic mixing in thermocapillary-driven microdroplets. *Phys. Fluids*, 17(3), 2005.

[16] O.M. F.R.S. Lord Rayleigh. Cxii. the problem of the whispering gallery. *Phil. Mag. Series 6*, 20(120):1001–1004, 1910.

[17] O.M. F.R.S. Lord Rayleigh. Ix. further applications of bessel's functions of high order to the whispering gallery and allied problems. *Phil. Mag. Series 6*, 27(157):100–109, 1914.

[18] Baron Rayleigh John William Strutt. *The theory of sound*. Macmillan and co., 1877.

[19] John D. Jackson. *Classical Electrodynamics*. John Wiley & Sons, 3rd edition, 1998.

[20] Richard L Sutherland. *Handbook of nonlinear optics*. CRC press, 2003.

[21] Michal Čada, Jaromír Pištora, and Montasir Qasymeh. *Optical Wave Propagation in Kerr Media*. INTECH Open Access Publisher, 2013.

[22] Andrea M. Armani, Rajan P. Kulkarni, Scott E. Fraser, Richard C. Flagan, and Kerry J. Vahala. Label-free, single-molecule detection with optical microcavities. *Science*, 317(5839):783–787, 2007.

[23] Anatolii Nikolaevich Oraevsky. Whispering-gallery waves. *Quant. Electron.*, 32(5):377–400, 2002.

[24] AB Matsko, AA Savchenkov, D Strekalov, VS Ilchenko, and L Maleki. Review of applications of whispering-gallery mode resonators in photonics and nonlinear optics. *IPN Progress Report*, 42:162, 2005.

[25] A. B. Matsko and V. S. Ilchenko. Optical resonators with whispering-gallery modes-part i: basics. *IEEE J. Sel. Top. Quant. Electron.*, 12(1):3–14, Jan 2006.

[26] V. S. Ilchenko and A. B. Matsko. Optical resonators with whispering-gallery modes-part ii: applications. *IEEE J. Sel. Top. Quant. Electron.*, 12(1):15–32, Jan 2006.

[27] Sai T Chu, Wugen Pan, Shinya Sato, Taro Kaneko, Brent E Little, and Yasuo Kokubun. Wavelength trimming of a microring resonator filter by means of a uv sensitive polymer overlay. *Photonics Technol. Lett., IEEE*, 11(6):688–690, 1999.

[28] AA Savchenkov, VS Ilchenko, T Handley, and L Maleki. Ultraviolet-assisted frequency trimming of optical microsphere resonators. *Opt. Lett.*, 28(8):649–650, 2003.

[29] F. Vollmer, D. Braun, A. Libchaber, M. Khoshsima, I. Teraoka, and S. Arnold. Protein detection by optical shift of a resonant microcavity. *Appl. Phys. Lett.*, 80(21), 2002.

[30] Frank Vollmer, Stephen Arnold, Dieter Braun, Iwao Teraoka, and Albert Libchaber. Multiplexed dna quantification by spectroscopic shift of two microsphere cavities. *Biophys. J.*, 85(3):1974–1979, 2003.

[31] S Arnold, M Khoshsima, I Teraoka, S Holler, and F Vollmer. Shift of whispering-gallery modes in microspheres by protein adsorption. *Opt. Lett.*, 28(4):272–274, 2003.

[32] Iwao Teraoka, Stephen Arnold, and Frank Vollmer. Perturbation approach to resonance shifts of whispering-gallery modes in a dielectric microsphere as a probe of a surrounding medium. *JOSA B*, 20(9):1937–1946, 2003.

[33] FC Blom, DR Van Dijk, HJWM Hoekstra, A Driessen, and Th JA Popma. Experimental study of integrated-optics microcavity resonators: Toward an all-optical switching device. *Appl. Phys. Lett.*, 71(6):747–749, 1997.

[34] John E Heebner and Robert W Boyd. Enhanced all-optical switching by use of a nonlinear fiber ring resonator. *Opt. Lett.*, 24(12):847–849, 1999.

[35] Suresh Pereira, Philip Chak, and JE Sipe. All-optical and gate by use of a kerr nonlinear microresonator structure. *Opt. Lett.*, 28(6):444–446, 2003.

[36] Vea Sandoghdar, F Treussart, J Hare, V Lefevre-Seguin, J-M Raimond, and S Haroche. Very low threshold whispering-gallery-mode microsphere laser. *Phys. Rev. A*, 54(3):R1777, 1996.

[37] Henry Power and Luiz C Wrobel. *Boundary integral methods in fluid mechanics*. Comput. Mech., 1995.

[38] C. Pozrikidis. Interfacial dynamics for stokes flow. *J. Comput. Phys.*, 169(2):250 – 301, 2001.

[39] Andrea Prosperetti and Gretar Tryggvason. *Computational methods for multiphase flow*. Cambridge, UK ; New York : Cambridge University Press, 2007.

[40] C. Pozrikidis. The instability of a moving viscous drop. *J. Fluid Mech.*, 210:1–21, 1 1990.

[41] Robert H. Davis. Buoyancy-driven viscous interaction of a rising drop with a smaller trailing drop. *Phys. Fluids*, 11(5), 1999.

[42] C. POZRIKIDIS. Effect of membrane bending stiffness on the deformation of capsules in simple shear flow. *J. Fluid Mech.*, 440:269–291, 8 2001.

[43] Peng Zhang, S. Jana, M. Giarra, P.P. Vlachos, and S. Jung. Paramecia swimming in viscous flow. *Eur. Phys. J. Special Topics*, 224(17):3199–3210, 2015.

[44] Hamza Chraïbi, Didier Lasseux, Eric Arquis, Rgis Wunenburger, and Jean-Pierre Delville. Simulation of an optically induced asymmetric deformation of a liquidliquid interface. *Eur. J. Mech. B. Fluids*, 27(4):419–432, 2008.

[45] Hamza Chraïbi, Didier Lasseux, Rgis Wunenburger, Eric Arquis, and Jean-Pierre Delville. Optohydrodynamics of soft fluid interfaces: optical and viscous nonlinear effects. *Eur Phys J E Soft Matter*, 32(1):43–52, 2010.

[46] Wolfgang Hackbusch. *Integral Equations: Theory and Numerical Treatment*. Birkhauser Verlag, Basel, Switzerland, Switzerland, 1995.

[47] Demetri Psaltis, Stephen R. Quake, and Changhuei Yang. Developing optofluidic technology through the fusion of microfluidics and optics. *Nature*, 442(7101):381–386, 2006.

[48] Uriel Levy and Romi Shamai. Tunable optofluidic devices. *Microfluid Nanofluidics*, 4(1-2):97–105, 2008.

[49] C. Monat, P. Domachuk, and B. J. Eggleton. Integrated optofluidics: A new river of light. *Nature Photon.*, 1(2):106–114, 2007.

[50] Se-Heon Kim, Jae-Hoon Choi, Seung-Kon Lee, Shin-Hyun Kim, Seung-Man Yang, Yong-Hee Lee, Christian Seassal, Philippe Regrency, and Pierre Viktorovitch. Optofluidic integration of a photonic crystal nanolaser. *Opt. Express*, 16(9):6515–6527, 2008.

[51] Zhenyu Li and Demetri Psaltis. Optofluidic dye lasers. *Microfluid Nanofluidics*, 4(1-2):145–158, 2007.

[52] Hongying Zhu, Ian M White, Jonathan D Suter, Paul S Dale, and Xudong Fan. Analysis of biomolecule detection with optofluidic ring resonator sensors. *Opt. Express*, 15(15):9139–9146, 2007.

[53] H. Rokhsari, T. J. Kippenberg, T. Carmon, and K. J. Vahala. Theoretical and experimental study of radiation pressure-induced mechanical oscillations (parametric instability) in optical microcavities. *IEEE J. Sel. Top. Quant. Electron.*, 12(1):96–107, 2006.

[54] Tobias J. Kippenberg and Kerry J. Vahala. Cavity opto-mechanics. *Opt. Express*, 15(25):17172–17205, 2007.

[55] T. J. Kippenberg and K. J. Vahala. Cavity optomechanics: Back-action at the mesoscale. *Science*, 321(5893):1172–1176, 2008.

[56] J. Hofer, A. Schliesser, and T. J. Kippenberg. Cavity optomechanics with ultrahigh-q crystalline microresonators. *Phys. Rev. A*, 82(3):031804, 2010.

[57] Siddharth Tallur, Suresh Sridaran, and Sunil A Bhave. A monolithic radiation-pressure driven, low phase noise silicon nitride opto-mechanical oscillator. *Opt. Express*, 19(24):24522–24529, 2011.

[58] Adrian Cho. Putting light's light touch to work as optics meets mechanics. *Science*, 328(5980):812–813, 2010.

[59] I.I. Komissarovak, G.V. Ostrovskaya, and E.N. Shedova. Light pressure induced deformations of a free liquid surface. *Opt Commun*, 66(1):15–20, 1988.

[60] Jian-Zhi Zhang and Richard K. Chang. Shape distortion of a single water droplet by laser-induced electrostriction. *Opt. Lett.*, 13(10):916–918, 1988.

[61] Alexis Casner, Jean-Pierre Delville, and Iver Brevik. Asymmetric optical radiation pressure effects on liquid interfaces under intense illumination. *J. Opt. Soc. Am. B*, 20(11), 2003.

[62] Gaurav Bahl, Kyu Hyun Kim, Wonsuk Lee, Jing Liu, Xudong Fan, and Tal Carmon. Brillouin cavity optomechanics with microfluidic devices. *Nat. Commun.*, 4, 2013.

[63] Mani Hossein-Zadeh and Kerry J. Vahala. Fiber-taper coupling to whispering-gallery modes of fluidic resonators embedded in a liquid medium. *Opt. Express*, 14(22):10800–10810, 2006.

[64] Alexandr Jon, Yasin Karadag, Michael Mestre, and Alper Kiraz. Probing of ultrahigh optical q-factors of individual liquid microdroplets on superhydrophobic surfaces using tapered optical fiber waveguides. *J. Opt. Soc. Am.*, 29(12):3240–3247, 2012.

[65] HM Lai, PT Leung, K Young, PW Barber, and SC Hill. Time-independent perturbation for leaking electromagnetic modes in open systems with application to resonances in microdroplets. *Phys. Rev. A*, 41(9):5187, 1990.

[66] J. R. Buck and H. J. Kimble. Optimal sizes of dielectric microspheres for cavity qed with strong coupling. *Phys. Rev. A*, 67(3):033806, 2003.

[67] H. Leitão, A. M. Somoza, M. M. Telo da Gama, T. Sottmann, and R. Strey. Scaling of the interfacial tension of microemulsions: A phenomenological description. *J. Chem. Phys.*, 105(7):2875, 1996.

[68] A. Datta, S. Kundu, M. Sanyal, J. Daillant, D. Luzet, C. Blot, and B. Struth. Dramatic enhancement of capillary wave fluctuations of a decorated water surface. *Phys. Rev. E*, 71(4), 2005.

[69] Vladimir B. Braginsky, Yuri I. Vorontsov, and Kip S. Thorne. Quantum nondemolition measurements. *Science*, 209(4456):547–557, 1980.

[70] P. A. Franken, A. E. Hill, C. W. Peters, and G. Weinreich. Generation of optical harmonics. *Phys. Rev. Lett.*, 7:118–119, Aug 1961.

[71] Anatoliy A. Savchenkov, Andrey B. Matsko, Dmitry Strekalov, Makan Mohageg, Vladimir S. Ilchenko, and Lute Maleki. Low threshold optical oscillations in a whispering gallery mode caf_2 resonator. *Phys. Rev. Lett.*, 93:243905, Dec 2004.

[72] J. U. Fürst, D. V. Strekalov, D. Elser, A. Aiello, U. L. Andersen, Ch. Marquardt, and G. Leuchs. Low-threshold optical parametric oscillations in a whispering gallery mode resonator. *Phys. Rev. Lett.*, 105:263904, Dec 2010.

[73] K. Sakai, D. Mizuno, and K. Takagi. Measurement of liquid surface properties by laser-induced surface deformation spectroscopy. *Phys. Rev. E*, 63:046302, Mar 2001.

[74] Shujiro Mitani and Keiji Sakai. Measurement of ultralow interfacial tension with a laser interface manipulation technique. *Phys. Rev. E*, 66:031604, Sep 2002.

[75] Romeric Pobre and Caesar Saloma. Radiation force on a nonlinear microsphere by a tightly focused gaussian beam. *Appl. Opt.*, 41(36):7694–7701, Dec 2002.

[76] Etienne Brasselet, Rgis Wunenburger, and Jean-Pierre Delville. Liquid optical fibers with a multistable core actuated by light radiation pressure. *Phys. Rev. Lett.*, 101(1):014501, 2008.

[77] David Tapp, Jonathan M. Taylor, Alex S. Lubansky, Colin D. Bain, and Buddhapriya Chakrabarti. Theoretical analysis for the optical deformation of emulsion droplets. *Opt. Express*, 22(4):4523–4538, Feb 2014.

[78] Yong Xu, Peng Zhang, Sunghwan Jung, and Aram Lee. Analysis of radiation pressure induced nonlinear optofluidics. *Opt. Express*, 22(23):28875–28889, Nov 2014.

[79] C. Pozrikidis. *Boundary Integral and Singularity Methods for Linearized Viscous Flow.* Cambridge University Press, 1992.

[80] G. Graziani. A boundary integral equation method for axisymmetric viscous flows. *Int. J. Engng Sci.*, 27(7):855–864, 1989.

[81] Robert W. Boyd. *Nonlinear Optics.* Academic, Amsterdam, 3rd edition, 2008.

[82] Michael A. Choma, Audrey K. Ellerbee, Changhuei Yang, Tony L. Creazzo, and Joseph A. Izatt. Spectral-domain phase microscopy. *Opt. Lett.*, 30(10):1162–1164, May 2005.

[83] Aram Lee, Baigang Zhang, Cheng Ma, Anbo Wang, and Yong Xu. Fiber-based white-light interferometry for nanoscale distance measurement and control. *Photonics Technol. Lett., IEEE*, 24(23):2136–2138, Dec 2012.

[84] Zhihao Yu and Anbo Wang. Fast white light interferometry demodulation algorithm for low-finesse fabry-pérot sensors. *Photonics Technol. Lett., IEEE*, 27(8):817–820, April 2015.

[85] Venkata R. Dantham, Stephen Holler, Curtis Barbre, David Keng, Vasily Kolchenko, and Stephen Arnold. Label-free detection of single protein using a nanoplasmonic-photonic hybrid microcavity. *Nano Lett.*, 13(7):3347–3351, 2013. PMID: 23777440.

[86] P Than, L Preziosi, D.D Josephl, and M Arney. Measurement of interfacial tension between immiscible liquids with the spinning road tensiometer. *J. Colloid Interface Sci.*, 124(2):552 – 559, 1988.

[87] Santi R. Palit. Thermodynamic interpretation of the eötvös constant. *Nature*, 177(4521):1180, 1956.

[88] Benny Davidovitch, Esteban Moro, and Howard A. Stone. Spreading of viscous fluid drops on a solid substrate assisted by thermal fluctuations. *Phys. Rev. Lett.*, 95:244505, Dec 2005.

[89] Klaus Mecke and Markus Rauscher. On thermal fluctuations in thin film flow. *J. Phys. Condens. Matter*, 17(45):S3515, 2005.

[90] W. Brouwer and R. K. Pathria. On the surface tension of liquid helium ii. *Phys. Rev.*, 163:200–205, Nov 1967.

[91] Armin Werber and Hans Zappe. Tunable microfluidic microlenses. *Appl. Opt.*, 44(16):3238–3245, Jun 2005.

[92] Peng Zhang, Sunghwan Jung, Aram Lee, and Yong Xu. Radiation-pressure-induced nonlinearity in microdroplets. *Phys. Rev. E*, 92:063033, Dec 2015.

[93] R. Wunenburger, B. Issenmann, E. Brasselet, C. Loussert, V. Hourtane, and J. P. Delville. Fluid flows driven by light scattering. *J. Fluid Mech.*, 666:273–307, 2010.

[94] Charles N. Baroud, Matthieu Robert de Saint Vincent, and Jean-Pierre Delville. An optical toolbox for total control of droplet microfluidics. *Lab Chip*, 7:1029–1033, 2007.

[95] Matthieu Robert de Saint Vincent, Rgis Wunenburger, and Jean-Pierre Delville. Laser switching and sorting for high speed digital microfluidics. *Appl. Phys. Lett.*, 92(15), 2008.

[96] S.H Lee and L.G Leal. The motion of a sphere in the presence of a deformable interface: Ii. a numerical study of the translation of a sphere normal to an interface. *J. Colloid Interface Sci.*, 87(1):81 – 106, 1982.

[97] I. S. Gradshteyn and I. M. Ryzhik. *Table of Integrals, Series, and Products (Eighth Edition)*. Academic Press, Boston, eighth edition, 2014.

Appendix A

Linear relation between Δp and $p_{\mathbf{opt}}$

We claim that the value of Δp is proportional to P_{WGM}. To prove this, let us assume a Δp^1 and p^1_{opt} (corresponding to P^1_{WGM}) result in an interface deformation $h^1(\theta)$ that satisfies Eq. (3.7) and volume conservation, i.e.,

$$h^{1\prime\prime}(\theta) + \cot(\theta) h^{1\prime}(\theta) + 2h^1(\theta) = -\frac{a}{\sigma}(\Delta p^1 + p^1_{\mathrm{opt}}). \tag{A.1}$$

If we change the WGM power to $\alpha P^1_{\mathrm{WGM}}$, then the optical pressure will be $\alpha p^1_{\mathrm{opt}}$, where α is a constant. We now show that $\alpha\Delta p^1$ gives a $h(\theta)$ that satisfies volume conservation. If we simply substitute $\alpha\Delta p^1$ and $\alpha p^1_{\mathrm{opt}}$ on the right hand side of Eq. (A.1), then the solution to Eq. (A.1) should be $\alpha h^1(\theta)$, because of the linearity of Eq. (A.1). Since $h^1(\theta)$ give zero volume change, $\alpha h^1(\theta)$ should also preserve the volume. Therefore, $\alpha\Delta p^1$ is the real Δp value. Here, we used the linearized volume change for small $h(\theta)$,

$$\Delta V/V = 3\int_0^{\pi/2} h(\theta)\sin(\theta)\, d\theta + \mathcal{O}(h^2). \tag{A.2}$$

Appendix B

Clebsch-Gordan expression for Γ_θ^{lm}

From the radiation pressure Eq. (3.3) and electric field Eq. (3.1) expressions, we can write the normalized pressure f_{lm} as,

$$f_{lm} = \frac{|\vec{X}_{lm}|^2}{|\vec{X}_{lm}|^2_{\max}}. \tag{B.1}$$

Note that the expression of Γ_θ^{lm} in Eq. (3.18) can be transformed into a surface integral,

$$\begin{aligned}\Gamma_\theta^{lm} &= -\frac{n_{co}a}{\lambda}\frac{1}{|\vec{X}_{lm}|^2_{\max}}\int_0^\pi |\vec{X}_{lm}|^2 Y_{20}(\theta)\sin(\theta)\,d\theta, \\ &= -\frac{n_{co}a}{2\pi\lambda}\frac{1}{|\vec{X}_{lm}|^2_{\max}}\iint |\vec{X}_{lm}|^2 Y_{20}\,d\Omega.\end{aligned} \tag{B.2}$$

With the Clebsch-Gordan expression for surface integral [65],

$$\begin{aligned}\iint |\vec{X}_{lm}|^2 Y_{LM}\,d\Omega = \left[1 - \frac{L(L+1)}{2l(l+1)}\right]\sqrt{\frac{2L+1}{4\pi}} \\ \times \langle L, l; M, m | l, m\rangle \langle L, l; 0, 0 | l, 0\rangle,\end{aligned} \tag{B.3}$$

Eq. (3.19) can be obtained with $L = 2, M = 0$. Equation. (3.22) can also be obtained by Eq. (B.3).

Appendix C

Derivation of the Greens functions in axisymmetric domain

We start by writing all the position, velocity and force variables in Eq. (4.3) in terms of their x, r and ϕ components. Without loss of generality, we assume $\boldsymbol{x}_0$ is located on the $\phi = 0$ plane, then the left-hand-side of Eq. (4.3) can be expressed as $\boldsymbol{u}(\boldsymbol{x}_0) = (u_x, u_r, u_\phi)$. Similarly, variables on the right-hand-side can be written as,

$$
\begin{aligned}
&\boldsymbol{x} = (x, r\cos\phi, r\sin\phi)\\
&\boldsymbol{x}_0 = (x_0, r_0, 0)\\
&\boldsymbol{n} = (n_x, n_r\cos\phi, n_r\sin\phi)\\
&\boldsymbol{f} = (f_x, f_r\cos\phi, f_r\sin\phi)\\
&\boldsymbol{F} = (0, -F_\phi\sin\phi, F_\phi\cos\phi)\\
&\boldsymbol{u} = (u_x, u_r\cos\phi, u_r\sin\phi) + (0, -u_\phi\sin\phi, u_\phi\cos\phi)\\
&\boldsymbol{s} = (x - x_0, r\cos\phi - r_0, r\sin\phi)\\
&s = |\boldsymbol{s}| = [(x - x_0)^2 + r^2 + r_0^2 - 2rr_0\cos\phi]^{1/2}.
\end{aligned}
\tag{C.1}
$$

Note that in Eq. (C.1), all the velocity and force components $(u_x, u_r, u_\phi, f_x, f_r, F_\phi)$ are functions of (x, r) only. The only terms that are ϕ-dependent are the Green's functions, which are pre-determined. We can thus integrate the Green's functions in Eq. (4.3) along the ϕ direction analytically to reduce the dimension of numerical integration.

The single layer integral in Eq. (4.3) can be calculate as,

$$\begin{aligned}
&\int_S G_{ji}(\boldsymbol{x}_0,\boldsymbol{x})f_i(\boldsymbol{x})\,dS = \int_S (G_{jx}f_x + G_{jy}f_y + G_{jz}f_z)\,dS \\
&= \int_S [G_{jx}f_x + (G_{jy}\cos\phi + G_{jz}\sin\phi)f_r]\,dS \\
&= \int_C \begin{bmatrix} M_{xx} & M_{xr} \\ M_{rx} & M_{rr} \\ M_{\phi x} & M_{\phi r} \end{bmatrix} \begin{Bmatrix} f_x \\ f_r \end{Bmatrix} dl, \qquad \text{(C.2)}
\end{aligned}$$

where

$$\begin{aligned}
&\begin{bmatrix} M_{xx} & M_{xr} \\ M_{rx} & M_{rr} \\ M_{\phi x} & M_{\phi r} \end{bmatrix} (\boldsymbol{x}_0,\boldsymbol{x}) \\
&= r\int_0^{2\pi} \begin{bmatrix} G_{xx} & G_{xy}\cos\phi + G_{xz}\sin\phi \\ G_{yx} & G_{yy}\cos\phi + G_{yz}\sin\phi \\ G_{zx} & G_{zy}\cos\phi + G_{zz}\sin\phi \end{bmatrix} d\phi. \qquad \text{(C.3)}
\end{aligned}$$

The integral of the Green's function over ϕ can be converted to elliptic integrals. For example,

$$\begin{aligned}
M_{xx} &= r\int_0^{2\pi} G_{xx}d\phi = r\int_0^{2\pi} (\frac{1}{s} + \frac{{d_x}^2}{s^3})d\phi \\
&= r[I_{10} + d_x^2 I_{30}], \qquad \text{(C.4)}
\end{aligned}$$

where $d_x = x - x_0$, and [79]

$$I_{mn}(d_x, r, r_0) = c_m \int_0^{\pi/2} \frac{(2\cos^2\omega - 1)^n}{(1 - k^2\cos^2\omega)^{m/2}} d\omega, \qquad \text{(C.5)}$$

with

$$c_m = \frac{4k^m}{(4rr_0)^{m/2}}, \quad k^2 = \frac{4rr_0}{{d_x}^2 + (r + r_0)^2}. \qquad \text{(C.6)}$$

The integral in Eq. (C.5) can be expressed by complete elliptic integrals of the first and second kind ($F(k)$ and $E(k)$, respectively) with the help of integral tables [97]. The values of $M_{\alpha\beta}$ for $\alpha, \beta = 1, 2$ are the same as those derived in literature [79]. We can also show that $M_{\phi x} = M_{\phi r} = 0$.

The double layer integral in Eq. (4.3) can be calculate as,

$$\begin{aligned}
&\int_S u_i(\boldsymbol{x})K_{ijm}(\boldsymbol{x},\boldsymbol{x}_0)n_m(\boldsymbol{x})\,dS(\boldsymbol{x}) \\
&= \int_S [u_x K_{xjm}n_m + u_\sigma(K_{yjm}n_m\cos\phi + K_{zjm}n_m\sin\phi) \\
&\quad + u_\phi(-K_{yjm}n_m\sin\phi + K_{zjm}n_m\cos\phi)]\,dS \\
&= \int_C Q_{j\beta\gamma}u_\beta n_\gamma\,dl, \qquad \text{(C.7)}
\end{aligned}$$

where in the last integral indices $j, \beta, \gamma = 1, 2, 3$, representing x, r, ϕ components. The value of $Q_{j\beta\gamma}$ in Eq. (C.7) can be expressed as (note $n_\phi = 0$),

$$\begin{aligned}
Q_{jxx} &= r \int_0^{\pi/2} K_{xjx}\, d\phi \\
Q_{jxr} &= r \int_0^{\pi/2} (K_{xjy} \cos\phi + K_{xjz} \sin\phi)\, d\phi \\
Q_{jrx} &= Q_{jxr} \\
Q_{jrr} &= r \int_0^{\pi/2} (K_{yjy} \cos^2\phi + 2K_{yjz} \sin\phi\cos\phi \\
&\quad + K_{zjz} \sin^2\phi)\, d\phi \\
Q_{j\phi x} &= r \int_0^{\pi/2} (-K_{yjx} \sin\phi + K_{zjx} \cos\phi)\, d\phi \\
Q_{j\phi r} &= r \int_0^{\pi/2} (-K_{yjy} \sin\phi\cos\phi \\
&\quad + K_{zjy}(\cos^2\phi - \sin^2\phi) + K_{zjz} \sin\phi\cos\phi)\, d\phi.
\end{aligned} \tag{C.8}$$

By substituting the Green's function Eq. (4.4) into Eq. (C.8) and with the help of Eq. (C.5), we can show that for $j, \beta, \gamma = 1, 2$, the expressions of $Q_{j\beta\gamma}$ are the same as derived in literature. We can also show that for the new terms associated with the ϕ component ($j = 3$ or $\beta = 3$),

$$Q_{\phi x\gamma} = Q_{\phi r\gamma} = Q_{x\phi\gamma} = Q_{r\phi\gamma} = 0, \quad (\gamma = 1, 2) \tag{C.9}$$

and

$$\begin{aligned}
Q_{\phi\phi x} &= 6r^2 r_0 d_x (I_{52} - I_{50}) \\
Q_{\phi\phi r} &= -6r^2 r_0 [r_0 (I_{53} - I_{51}) + r(I_{50} - I_{52})].
\end{aligned} \tag{C.10}$$

Similarly, the volume integral in Eq. (4.3) can be simplified as,

$$\begin{aligned}
&\int_V G_{ji}(\boldsymbol{x}_0, \boldsymbol{x}) F_i(\boldsymbol{x})\, dV(\boldsymbol{x}) \\
&= \int_A \left[r \int_0^{2\pi} G_{ji}(\boldsymbol{x}_0, \boldsymbol{x}) F_i(\boldsymbol{x})\, d\phi \right] dA(\boldsymbol{x}) \\
&= \int_A r M_{j\phi}(\boldsymbol{x}_0, \boldsymbol{x}) F_\phi\, dA(\boldsymbol{x}),
\end{aligned} \tag{C.11}$$

where we have defined

$$\begin{aligned}
&M_{j\phi}(\boldsymbol{x}_0, \boldsymbol{x}) \\
=&r \int_0^{2\pi} [-G_{j2}(\boldsymbol{x}_0, \boldsymbol{x}) \sin\phi + G_{j3}(\boldsymbol{x}_0, \boldsymbol{x}) \cos\phi]\, d\phi.
\end{aligned} \tag{C.12}$$

It is easy to show that

$$M_{x\phi} = M_{r\phi} = 0, \tag{C.13}$$

and

$$\begin{aligned}
&M_{\phi\phi}(\boldsymbol{x}_0, \boldsymbol{x}) \\
=&r \int_0^{2\pi} [-G_{32}(\boldsymbol{x}_0, \boldsymbol{x}) \sin\phi + G_{33}(\boldsymbol{x}_0, \boldsymbol{x}) \cos\phi]\, d\phi \\
=&r \int_0^{2\pi} [-\frac{r(r\cos\phi - r_0)}{s^3} \sin^2\phi \\
&\qquad + \left(\frac{1}{s} + \frac{r^2 \sin^2\phi}{s^3}\right) \cos\phi]\, d\phi \\
=&r[I_{11} + rr_0(I_{30} - I_{32})].
\end{aligned} \tag{C.14}$$

It is obvious now that Eqs. (C.2), (C.7) and (C.11) lead to Eq. (4.5), and all the Green's functions in the axisymmetric domain are explicitly determined in this section.

Appendix D

Singularity of Green's functions

Let us define the distance between $\boldsymbol{x}$ and $\boldsymbol{x}_0$ on a ϕ = constant plane as $\boldsymbol{d} = (d_x, d_r) = (x - x_0, r - r_0)$ and $d = ((x - x_0)^2 + (r - r_0)^2)^{1/2}$. It has been shown in literature [79, 46] that as $\boldsymbol{x} \to \boldsymbol{x}_0$, $M_{xx}, M_{rr} \to -2\ln(d)$, while M_{xr}, M_{rx} and $Q_{\alpha\beta\gamma}n_\gamma$ are finitely bounded, for $\alpha, \beta, \gamma = 1, 2$. We now show that the newly derived nontrivial terms in this work, $M_{\phi\phi}$ and $Q_{\phi\phi\gamma}n_\gamma$, also exhibit $\mathcal{O}(\ln(d))$ type singularity.

From Eq. (C.5) and with the help of [97], we can show that

$$\begin{aligned} I_{11} &= \frac{c_1}{k^2}[-2E - (k^2 - 2)F] \\ I_{30} - I_{32} &= \frac{4c_3}{k^4}[-2E - (k^2 - 2)F], \end{aligned} \tag{D.1}$$

where F and E are complete elliptic integrals of the first and second kind, whose definition and asymptotic behaviors are,

$$\begin{aligned} F(k) &= \int_0^{\pi/2} \frac{1}{(1 - k^2\cos^2\xi)}\, d\xi \to -\ln(d), \\ E(k) &= \int_0^{\pi/2} (1 - k^2\cos^2\xi)\, d\xi \to 1, \end{aligned} \tag{D.2}$$

Therefore, Eq. (C.14) leads to

$$M_{\phi\phi} = -\frac{4}{k}\sqrt{\frac{r}{r_0}}[2E + (k^2 - 2)F] \to -4\ln(d). \tag{D.3}$$

Similarly, we can show

$$\begin{aligned} I_{52} - I_{50} &= c_5 \left[\frac{8}{3k^4} F + \frac{4(k^2-2)}{3k^4 k'} E \right], \\ I_{53} - I_{51} &= \frac{4c_5}{3k^6 k'^2} [-8k'^2(k^2-2)F \\ &\qquad - (k^4 - 16k^2 + 16)E], \end{aligned} \tag{D.4}$$

with $k'^2 = 1 - k^2$. The values of $Q_{\phi\phi\gamma}(\gamma = 1, 2)$ exhibit strong singularities ($\sim 1/d^2$). However, the product of $Q_{\phi\phi\gamma}$ and n_γ, i.e., $q_{33} = Q_{\phi\phi\gamma} n_\gamma$, may exhibit weaker singularity. Here we compute q_{33} explicitly,

$$\begin{aligned} q_{33} &= Q_{\phi\phi x} n_x + Q_{\phi\phi r} n_r \\ &= 6r^2 r_0 [(d_x n_x + r n_y)(I_{52} - I_{50}) + r_0 n_y (I_{51} - I_{53})] \\ &= \frac{8r^2 r_0 c_5}{k^6} [g_F(k) F + g_E(k) E], \end{aligned} \tag{D.5}$$

where g_F and g_E are functions k, which can be simplified as,

$$\begin{aligned} g_F(k) &= 2[(d_x n_x + r n_y + 4 r_0 n_y) k^2 - 8 r_0 n_y] \\ &\to 2(d n_x - 3 r_0) n_y \qquad (\boldsymbol{x} \to \boldsymbol{x}_0) \\ g_E(k) &= \frac{1}{k'^2} [(d_x n_x + r n_y + r_0 n_y) k^4 \\ &\quad - (d_x n_x + r n_y + r_0 n_y) k^2 + 16 r_0 n_y] \\ &= \frac{1}{k'^2} [-(d_x n_x + d_r n_y) k^2 + 16 r_0 n_y k'^2 - 2 r_0 n_y k^2 k'^2]. \end{aligned} \tag{D.6}$$

Note that in the last equation of Eq. (D.6), $\boldsymbol{d}$ becomes orthogonal to $\boldsymbol{n}$ as $\boldsymbol{x} \to \boldsymbol{x}_0$, and $\boldsymbol{d} \cdot \boldsymbol{n} \sim d^2$. Therefore g_E is non-singular. Combining Eqs. (D.2), (D.5) and (D.6), and note $d \ln(d) \to 0$ as $d \to 0$, we have,

$$q_{33} \to \frac{8 r_0^3 c_5}{k^6} (6 r_0 n_y \ln(d)) \to \frac{6 n_y}{r_0} \ln(d). \tag{D.7}$$

In the present work $\boldsymbol{x}$ and $\boldsymbol{x_0}$ are located on a circle with unit radius; in this case we have $q_{33} \to 6 \ln(d)$.

The presence of $\psi \ln(d)$ ($\psi = -2, -4$ or 6) singularities may cause large numerical integration error. To reduce the numerical error, the singularity can be subtracted from the singular Green's functions to make the integration non-singular. The analytic integral of $\psi \ln(d)$ should then be added back to the non-singular integral. This technique has also been used in literature and proved to be highly accurate [96, 79, 41, 46].